Dissertation

submitted to the
Combined Faculty for the Natural Sciences and Mathematics
of the Heidelberg University, Germany
for the degree of
Doctor of Natural Sciences

Put forward by

Kim Marina Holm
born in: Göttingen, Germany

Oral examination: June 16, 2021

Absorbed dose to water measurements in the SOBP of a clinical carbon-ion beam using water calorimetry

Referees: Prof. Dr. Joao Seco
Prof. Dr. Oliver Jäkel

Messung der im Wasser absorbierten Dosis im SOBP eines klinischen Kohlenstoffstrahls mit Hilfe von Wasserkalorimetrie

Die Dosimetrie bezogen auf die Wasser-Energiedosis erreicht in Kohlenstoffstrahlen bisher nicht die gleiche Genauigkeit wie in hochenergetischen Photonenstrahlen. Dies ist größtenteils durch die Standardunsicherheit des Korrektionsfaktors für die Strahlenqualität k_Q bedingt. Aufgrund fehlender experimenteller Daten basiert k_Q hauptsächlich auf theoretischen Berechnungen und weist dadurch eine dreimal höhere Standardunsicherheit auf als in Photonenstrahlen. Um diese Unsicherheit zu reduzieren, wurden experimentelle k_Q-Faktoren bereits für den Eingangskanal eines monoenergetischen Kohlenstoffstrahls bestimmt. Im Rahmen dieser Arbeit werden nun erstmals k_Q-Faktoren für den Spread-Out-Bragg-Peak (SOBP) eines Kohlenstoffstrahls präsentiert. Dazu wurde die Wasser-Energiedosis in einem zuvor gut charakterisierten Bestrahlungsfeld mit Hilfe von Wasserkalorimetrie bestimmt. Um diese Messungen in gescannten Kohlenstoffstrahlen durchführen zu können, wurde der SOBP passiv mit einem statischen 2D-Reichweitenmodulator erzeugt. Basierend auf den kalorimetrischen Messungen konnten Ionisationskammern direkt kalibriert und dabei kammerspezifische k_Q-Faktoren mit einer relativen Standardunsicherheit von 0,7 % bestimmt werden. Diese signifikante Reduzierung der Unsicherheit im Vergleich zu berechneten Werten ermöglicht es, die Gesamtunsicherheit in der Ionisationskammer-basierten Dosimetrie für klinische Kohlenstoffstrahlen drastisch zu verringern.

Absorbed dose to water measurements in the SOBP of a clinical carbon-ion beam using water calorimetry

Up til now, the dosimetry in terms of absorbed dose to water in carbon-ion beams has not reached the same level of accuracy as in high-energy photon beams. This is strongly influenced by the standard uncertainty of the beam quality correction factor k_Q. Due to a lack of experimental data, k_Q is mainly based on theoretical calculations showing a three times higher uncertainty than in photon beams. In order to reduce this standard uncertainty, experimental k_Q factors have been determined for the entrance channel of a monoenergetic carbon-ion beam. Within this thesis, k_Q factors are now presented for the spread-out Bragg peak (SOBP) of a carbon-ion beam for the first time. Therefore, the absorbed dose to water in a previously well-characterized irradiation field was determined by means of water calorimetry. To be able to perform these measurements in scanned carbon-ion beams, the SOBP was passively modulated using a static 2D range modulator. Based on the water calorimetric measurements, ionization chambers could be calibrated directly, determining chamber-specific k_Q factors with a relative standard uncertainty of 0.7 %. This significant reduction in uncertainty compared to calculated values gives the chance to drastically decrease the overall uncertainty in IC-based dosimetry for clinical carbon-ion beams.

List of publications

Parts of this work have been published in the following references:

[1] K.M. Holm, U. Weber, Y. Simeonov, A. Krauss, O. Jäkel and S. Greilich
2D range modulator for high-precision water calorimetry in scanned carbon-ion beams
Physics in Medicine and Biology, 65:215003, 2020

[2] K.M. Holm, E. Yukihara, M.F. Ahmed, S. Greilich and O. Jäkel
Triple channel analysis of Gafchromic EBT3 irradiated with clinical carbon-ion beams
Submitted to Physica Medica, under review

[3] K.M. Holm, O. Jäkel and A. Krauss
Water calorimetry-based k_Q factors for Farmer-type ionization chambers in the SOBP of a carbon-ion beam
Submitted to Physics in Medicine and Biology, under review

Conference contributions:

K.M. Holm, J.-M. Osinga-Blättermann, Y. Simeonov, U. Weber, S. Brons, O. Jäkel, S. Greilich and A. Krauss. Bestimmung von k_Q-Faktoren für Ionisationskammern im SOBP eines Kohlenstoffstrahls (Poster). *DGMP Tagung, Nürnberg (Germany)*, 2018

K.M. Holm, U. Weber, Y. Simeonov, S. Brons, O. Jäkel, U. Ankerhold, S. Greilich and A. Krauss. Absorbed dose to water measurements in the SOBP of a clinical carbon ion beam using water calorimetry (Poster). *IDOS, Vienna (Austria)*, 2019

K.M. Holm, U. Weber, Y. Simeonov, S. Brons, S. Greilich and A. Krauss. Bestimmung der Wasserenergiedosis im SOBP eines ^{12}C-Strahls: Optimierung des Bestrahlungsfeldes (Poster). *DGMP Tagung, Stuttgart (Germany)*, 2019

K.M. Holm, U. Weber, Y. Simeonov, O. Jäkel, S. Greilich and A. Krauss. Absorbed dose to water measurements in the SOBP of a ^{12}C beam using water calorimetry (Talk). *PTCOG, online meeting*, 2020

Contents

List of abbreviations

2DRM	Two-dimensional range modulator
BAMS	Beam application monitoring system
BP	Bragg peak
DKFZ	German Cancer Research Center
DTA	Distance to agreement
FWHM	Full width at half maximum
GSI	Gesellschaft für Schwerionenforschung
HIT	Heidelberg Ion-beam Therapy Center
IAEA	International Atomic Energy Agency
IC	Ionization chamber
LET	Linear energy transfer
LINAC	Linear accelerator
MC	Monte Carlo
MWPC	Multi-wire proportional chamber
PMMA	Poly methyl methacrylate (acrylic glass)
PTB	Physikalisch-Technische Bundesanstalt
px	Pixel
QA	Quality assurance
RBE	Relative biological effectiveness
ROI	Region of interest
SOBP	Spread-out Bragg peak
vx/pin	Voxel per pin
WET	Water-equivalent thickness

1 Introduction

The radiation therapy with carbon-ion beams has become an attractive tool for cancer treatment [4, 5, 6], as it offers both physical and biological advantages compared to conventional high-energy photon radiotherapy. Due to a low scattering behaviour and a defined range in material with the highest energy deposition in the Bragg peak (BP) (see Figure 1, mono-energet. ^{12}C), carbon ions offer the opportunity for a very precise spatial dose deposition, allowing a greater local tumor control while sparing the healthy tissue [7]. Furthermore, carbon ions show an enhanced relative biological effectiveness (RBE) due to an increased linear energy transfer (LET) and thus a higher ionization density [8, 9].

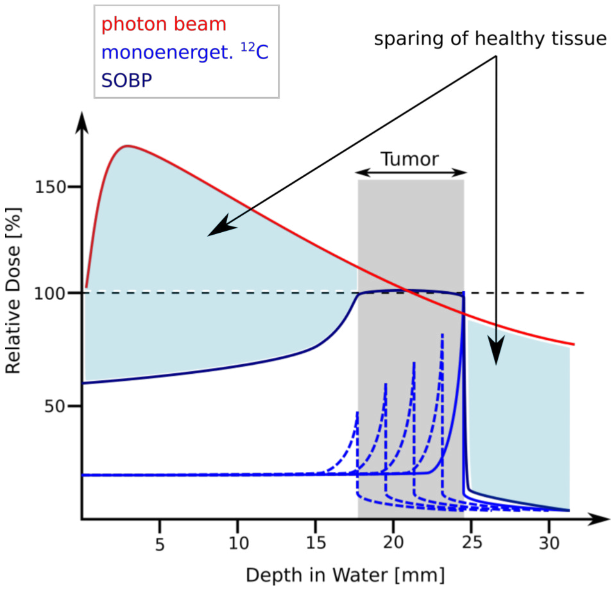

Figure 1: Schematic illustration of the superposition of mono-energetic carbon-ion beams to a SOBP for the treatment of a certain tumor volume (gray area). The depth dose curves of the single carbon-ion beams (blue, partially dashed lines) as well as the resulting SOBP (dark blue) are shown in comparison to the depth dose distribution of a photon beam (red). The healthy tissue that can be spared in the carbon-ion treatment compared to the photon irradiation is indicated by the light blue areas.

In consequence, this precise tool for cancer treatment requires a very accurate dosimetry to verify and ensure the irradiation quality. However, the dosimetry for carbon-ion beams has not reached the same level of accuracy as for photon beams so far. The standard uncertainty for dosimetry in terms of the absorbed dose to water in clinical photon beams using calibrated ionization chambers (ICs) is about 1 % [10, 11, 12]. For carbon-ion beams, it is about three times higher [10], which is mainly caused by a high standard uncertainty of the correction factor for the beam quality k_Q [6].

As ICs are calibrated at a reference beam quality Q_0 (usually ^{60}Co), the absorbed dose to water to be measured at the user's beam quality Q needs to be corrected for the different response of the IC to the beam qualities Q and Q_0 by applying the beam quality correction factor k_Q. Due to a lack of experimental data in carbon-ion beams, k_Q values are primarily based on theoretical calculations, as stated in the international recommendations on reference dosimetry, the International Code of Practice for the Dosimetry of External Radiotherapy Beams TRS-398 [10], as well as in the German DIN 6801-1 [13]. Hereby, different assumptions for the influencing quantities are being made resulting in a standard uncertainty for k_Q of 2.8 % (TRS [10]) or rather 2.2 % (DIN [13]). In contrast, for photons this is 1.0 % [10]; if experimentally determined values are also taken into account, it is even lower (0.6 %) [14].

Direct experimental determinations of k_Q values by means of water calorimetry for different ionization chambers have been presented for medium-energy x-rays [15], high-energy photons [16, 17, 18], electron beams [19] as well as for passively scattered [20] and scanned pulsed protons [21]. k_Q factors based on Monte Carlo (MC) simulations have also been presented for photon [22, 23], electron [24, 25] and proton beams [26]. In contrast, experimental and MC-based data for carbon-ion beams is very rare. Water calorimetry-based absorbed dose to water values have been presented for example by Brede *et al.* [27]; Burigo *et al.* [28] performed MC simulations to calculate stopping power ratios and k_Q factors for carbon-ion beams based on the ICRU 90 key data [29].

Osinga *et al.* [30] experimentally determined k_Q factors for two Farmer-type ICs in the entrance channel of a mono-energetic carbon-ion beam using the water calorimeter designed at Physikalisch-Technische Bundesanstalt (PTB) [31, 15]. The entrance channel, defined at a shallow depth of a mono-energetic field, is characterized by a relatively low LET. Here, an overall standard uncertainty for k_Q of 0.8 % was achieved. Performing a cross-calibration, k_Q factors for a further eight different cylindrical ICs and three different plane-parallel ICs were determined with a standard uncertainty of 1.1 % [32]. These measurements were performed at the Heidelberg Ion-Beam Therapy Center (HIT) using a raster scanning beam delivery system, since Jäkel *et al.* [33] recommended measurements at the entrance channel of a mono-energetic beam for the calibration of the beam monitoring system of such a scanning system.

Nevertheless, as the target region of carbon-ion radiotherapy is irradiated with a spread-out Bragg peak (SOBP, see Figure 1), additional verification of the delivered dose by measurements at the SOBP is needed. This makes a precise dosimetry essential also in this region. Within this thesis, k_Q factors for the SOBP of a carbon-ion beam were determined for the first time. Measurements were performed at the HIT. As the SOBP is characterized by a higher LET compared to the entrance channel, possible dependencies of k_Q on the LET should be observed. The reduced standard uncertainty of the experimental determined k_Q values that could be achieved may contribute to a reduction of the overall uncertainty in carbon-ion radiotherapy.

To be able to determine k_Q factors, first, a suitable irradiation field was needed. An irradiation technique using a static 2D range modulator (2DRM) was developed and optimized in terms of field size and homogeneity achieving an irradiation time suitable for water calorimetric measurement. The resulting dose distribution was characterized in detail in order to verify its applicability for water calorimetry and as a data base to determine correction factors and uncertainty contributions for the determination of k_Q.
A reliable measurement tool as well as an efficient setup were needed to be able to measure a 3D dose distribution accurately and within a reasonable time. For this purpose, a setup was developed to move an IC array inside a water phantom remote-controlled in depth. Additional film measurements were performed to verify the spatial resolution of the array. For a comprehensive comparison of film and IC array data, the film was corrected for non-dose dependent artifacts by successfully applying the triple channel analysis to carbon-ion irradiated film for the first time.
Water calorimetric and ionometric measurements were performed in order to determine k_Q factors as well as their overall standard uncertainty.

2 Background

In this chapter, an overview of the interaction processes of heavy charged particle with matter and their description is presented. An introduction to dosimetric concepts to measure the absorbed dose to a medium is given including the theory of IC-based dosimetry as well as water calorimetry. The practical dosimetry using calibrated ICs as well as the current status of reference dosimetry in carbon-ion beams is presented.

2.1 Interaction of charged particles with matter

Unless otherwise indicated, the following explanations are taken from [34, 35].

When charged particles enter matter, several interaction processes occur leading to an energy loss of the particle, a slowing down, scattering and fragmentation processes. Heavy charged particles (such as carbon ions) slowly loose their energy in matter until they finally come to rest. The total mean energy lost during all interactions per distance in matter travelled is called the **stopping power** S; it can be divided into three components:

$$S = \overline{dE}/dx = S_{col} + S_{rad} + S_{nuc}. \tag{1}$$

The electronic stopping power S_{col} describes the energy loss due to collisions with atomic electrons. The energy loss due to the deflection of the primary particle from a target nucleus leading to the emission of a photon, the so-called Bremsstrahlung, is given by the radiative stopping power S_{rad}. It strongly depends on the mass of the primary particle and is only relevant for electrons, whereas it can be neglected for heavy charged particles at therapeutic energies. The nuclear stopping power S_{nuc} describes the energy loss due to elastic Coulomb scattering of the particles at the target nuclei, this effect is negligible for energies $> 1\,\mathrm{MeV}$. Energy loss due to inelastic scattering with target nuclei leading to the production of secondary particles (fragments) is not included in the stopping power. For clinically relevant energies of carbon ions (about 90 MeV/u up to 430 MeV/u), the energy loss is dominated by the electronic stopping power. It is well described by the relativistic Bethe formula derived by Hans Bethe [36]:

$$S \approx S_{col} = \rho \cdot k \cdot \frac{Z}{A} \cdot \frac{z^2}{\beta^2} \cdot L(\beta), \tag{2}$$

with a constant factor $k \approx 0.3071\,\mathrm{MeV{\cdot}cm^2/g}$, the reduced electron density Z/A of the target material, and the charge z and velocity $\beta = v/c$ of the projectile. The rest function $L(\beta)$ includes additional dependencies on the velocity and the mean excitation potential I:

$$L(\beta) = \frac{1}{2} ln \left(\frac{2 m_e c^2 \beta^2}{1 - \beta^2} \right) - \beta^2 - ln(I). \tag{3}$$

The Bethe formula can be extended by additional correction terms which take e.g. the impact of the atomic shell structure into account.

From Equation 2, it can be seen that for a decreasing energy, which means a slowing down of the projectile, the stopping power increases dramatically as $S \sim 1/v^2$. This leads to a increased deposition of energy at the end of the projectiles' track resulting in the characteristic depth dose distribution with the so-called Bragg peak, as shown in Figure 1 (depth-dose curve of the mono-energetic ^{12}C beam). As $S \sim Z^2$, the stopping power also increases dramatically with increasing charge of the projectile, meaning a carbon ion will deposit more energy in the target medium than e.g. a proton at the same velocity. Due to electron capture at low velocities, Z is not constant for heavy charged particles, leading to a decrease of the stopping power at a certain energy of the projectile. If restricted to secondary particles with an energy below a certain threshold Δ, the electronic stopping power for charged particles equals the **linear energy transfer (LET)** L_Δ. For $\Delta \to \infty$, the limit of the LET is the unrestricted electronic stopping power:

$$\lim_{\Delta \to \infty} L_\Delta = S_{col}. \tag{4}$$

The LET describes the local energy deposition within a certain area around the primary particle track. For heavy charged particles, many low-energy and therefore short-range secondary electrons are produced within several interaction processes with the target material. This leads to a very local energy deposition and a high LET.

Due to many interactions with low energy deposition, a continuous slowing down process while travelling through an absorber can be assumed for heavy charged particles. Following that, the range of a particle in matter can be calculated by integrating the inverse stopping power:

$$R(E) = \int_E^0 \frac{1}{S(E')} dE'. \tag{5}$$

In practice, one uses the **practical range** of a beam. For carbon ions it is defined as the depth in water at which the value of the percentage depth dose distribution after the Bragg peak (corresponding to 100 % dose) has dropped to 50 % [13]. Due to a low scattering behaviour of the ions, this practical range is a good approximation of the particle's range R (Equation 5).

The range straggling σ_{range} is proportional to $1/\sqrt{M}$, with M denoting the projectile's mass. This means that for heavy charged particles with high mass M, the range straggling is very low and the particles' ranges and track length match well. Multiple scattering leading to range straggling, as it occurs in thick absorbers, is described by the Molière theory [37, 38] which provides in a first approximation a normal distribution of the scattering angles. The range straggling is determined by an energy straggling which leads to a broadening of the initial beam energy to a normally distributed spectrum.

The path length of the particle is often stated in water-equivalent units, converting the range in e.g. human tissue into the corresponding range in water as it is needed for analytical dose planning algorithms [39]. The **water-equivalent path length (WEPL)** is defined as the ratio of the mean particle range in a medium m and in water. It can be derived from the stopping power ratios in both media. Experimentally, it is determined via range in water measurements using e.g. the PTW Peakfinder (Chapter 3.2.3) as described by Jäkel *et al.* [40]. First, the depth dose distribution of a mono-energetic beam is measured without any additional material in the beam's path. For a second measurement, a material m of thickness d_m is positioned in the beam path. The Bragg peak's positions r_w (without material) and r_m (with material) for both measurements are determined, the WEPL then results from:

$$\text{WEPL} = \frac{r_w - r_m}{d_m}. \tag{6}$$

The material-specific property often specified is the **water-equivalent thickness (WET)**, which is defined as $\text{WET}_m = \text{WEPL}_m \cdot d_m$.

If the projectile's energy is high enough to overcome the target nucleus' Coulomb wall, nuclear interactions can take place. These interactions are very short-ranged, mediated by the strong interaction. In this process, fragments of both the projectile and the target are produced. The resulting fragment spectrum effects the depth dose distribution (resulting in the fragmentation tail), the biological efficiency, the response of detectors used, as well as dosimetrical correction factors such as k_Q.

2.2 Dosimetry

Unless otherwise indicated, the following explanations are taken from [34, 41].

The main quantity of interest in radiation therapy is the absorbed dose D which is defined as the mean energy $d\overline{E}$ absorbed per unit mass dm to a volume dV with the density ρ:

$$D = \frac{d\overline{E}}{dm} = \frac{d\overline{E}}{\rho \cdot dV}. \tag{7}$$

Its SI unit of measure is Gray (Gy): 1 Gy= 1 J/kg. Dosimetry is the field of representation and measurement of absorbed dose.

2.2.1 IC-based dosimetry

The basic concept for the determination of the absorbed dose to a medium according to DIN 6800-1 [42] is the probe method: A probe is inserted into the medium and irradiated together with it. The probe most commonly used for absolute reference dosimetry are air-filled ionization chambers (ICs). An IC consists of an anode and a cathode separated by an active medium (air) between which an operating voltage is applied. Within the active medium, free charges are created by the interaction between the radiation and the medium, which are collected by the applied electric field. The resulting current is measured by an electrometer as the IC's signal M; the absorbed dose D to the medium is determined from the signal M. To this end, corrections are needed due to the probe's material and components disturbing the irradiation field, or its measurement volume leading to a volume averaged signal. In reference dosimetry, the medium used is water; therefore, the absorbed dose to the medium will be referred as D_w.

To convert the probe's signal M to the absorbed dose to the medium D_w under reference conditions, first, M is corrected for the dependence on the current air density (under temperature T and air pressure p) using the correction factor k_ρ:

$$k_\rho = \frac{p_0}{p}\frac{T}{T_0}, \tag{8}$$

with $p_0 = 101.325\,\mathrm{kPa}$ and $T_0 = 293.15\,\mathrm{K}$ as reference condition. This gives the corrected signal $M_{corr} = M \cdot k_\rho$. Additional corrections needed for IC dosimetry, that are not included in M_{corr}, are described in Chapter 3.5.2. A possible background $M_0 \neq 0$ is considered during the measurement by performing a zero adjustment of the electrometer. The absorbed dose to the probe D_{det}, which includes the influence of all probe's components, is given by introducing an intrinsic energy dependence factor k_{intr}

$$D_{det} = k_{intr}(Q) \cdot k_{il} \cdot M_{corr}, \tag{9}$$

with

$$k_{intr} = \frac{w/e}{\rho V}. \tag{10}$$

Hereby, w/e is the mean energy needed to produce an ion pair in air, also referred to as W_{air} [10]; ρV is the mass air in the measurement volume. k_{il} is the intrinsic linearity factor describing the deviation between D_{det} and M_{corr}; if k_{il} is dose-independent, a linear detector response is given.

To determine the absorbed dose to the medium D_w from D_{det}, a dose conversion factor f for the given beam quality Q and measurement conditions C (field size, measurement depth, etc.) is needed:

$$f(Q,C) = \left(\frac{D_w}{D_{det}}\right)_{Q,C} \tag{11}$$

If the following conditions (Bragg-Gray conditions) are fulfilled, the dose conversion factor can be calculated according to the Bragg-Gray cavity theory, which was developed by Louis Harold Gray, William Henry Bragg and William Lawrence Bragg in 1936:

1. The dose inside the probe is only mediated by electrons passing the probe, only the electronic stopping power influences the energy transfer.

2. The electrons' fluence inside the probe is identical to the one in the medium, the probe does not disturb the fluence.

For a known electron fluence spectrum $\varPhi_{E,m}$, the absorbed dose inside the probe D_m (assuming that all probe's components are of the same material as the medium) can be calculated via:

$$D_m = \int \varPhi_{E,m} \left(\frac{S_{el}}{\rho}\right)_m dE, \tag{12}$$

with $\left(\frac{S_{el}}{\rho}\right)_m$ the mass electron stopping power of the measuring medium inside the probe. Introducing a mean mass electron stopping power with respect to the fluence spectrum inside the probe

$$\overline{\left(\frac{S_{el}}{\rho}\right)_m} = \frac{\int \Phi_{E,m} \left(\frac{S_{el}}{\rho}\right)_m dE}{\int \Phi_{E,m} dE}, \tag{13}$$

the absorbed dose is given by

$$D_m = \overline{\left(\frac{S_{el}}{\rho}\right)_m} \cdot \Phi_m, \tag{14}$$

using $\int \Phi_{E,m} dE = \Phi_m$.
For the medium which the absorbed dose shall be determined for, this is

$$D_w = \overline{\left(\frac{S_{el}}{\rho}\right)_w} \cdot \Phi_w. \tag{15}$$

Assuming a very small probe to fulfill the Bragg-Gray conditions, the fluence inside and outside the probe remains unchanged: $\Phi_m = \Phi_w$. It follows

$$f = \frac{D_w}{D_m} = \overline{\left(\frac{S_{el}}{\rho}\right)_w} \Bigg/ \overline{\left(\frac{S_{el}}{\rho}\right)_m}. \tag{16}$$

For the medium water and the probe's material air (as given for air-filled ICs), this conversion factor is denoted as $f = s^{BG}_{w,a}$.

As Equation 16 does not take δ-electrons with energies high enough to leave the probe's material into account, but considers these energies in the stopping power $\overline{\left(\frac{S_{el}}{\rho}\right)_m}$, modifications to the Bragg-Gray theory have to be made. These were introduced by Spencer and Attix in 1955 [43, 44]:

1. An energy-restricted electronic stopping power L_Δ was introduced excluding the high-energy δ-electrons which leave the probe's volume. In addition, an extended fluence Φ' was used which considers the δ-electrons' energy contribution.
2. It was distinguished between those electrons leaving the probe's material and those stopping inside the probe by defining an energy threshold Δ, as well as a so-called track-end term TE including the fraction of energy absorption by electrons with an energy $E \leq \Delta$.

With these modifications the dose conversion factor according to Spencer-Attix follows as

$$s^{SA}_{w,a} = \frac{\int_\Delta^{E_{max}} \Phi'_{E,w} \cdot (L_\Delta/\rho)_w + TE_w}{\int_\Delta^{E_{max}} \Phi'_{E,a} \cdot (L_\Delta/\rho)_a + TE_a}. \tag{17}$$

In reality, the Bragg-Gray conditions are not completely fulfilled, the insertion of a probe to a medium will always at least slightly change the fluence spectrum. To consider this perturbation of the spectrum at the measurement position, an additional, chamber-specific perturbation factor p_Q is introduced:

$$f(Q) = \left(s_{w,a}^{SA}\right)_Q \cdot p_Q. \tag{18}$$

2.2.2 Water calorimetry

Another and the most direct approach for the determination of the absorbed dose to water, even though it is usually not suitable for routine clinical use, is water calorimetry [6]. Hereby, the radiation-induced rise in temperature ΔT at a certain point inside a water phantom is measured. The absorbed dose to water $D_{w,Q}$ for the beam quality Q in which the measurement is performed is determined via

$$D_{w,Q} = \Delta T \cdot c_p \cdot \prod_i k_i, \tag{19}$$

with c_p denoting the specific heat capacity of water of 4206.8 J/(kg K) [45]. The k_i's indicate the different correction factors that have to be applied in order to correct for several effects such as heat conduction effects, the heat defect (describing the amount of deposited energy which does not appear as heat due to chemical reactions occurring) and other corrections due to the calorimeter's technical structure. These corrections are described in detail in Chapter 3.4.2.

For a reliable water calorimetric determination of the absorbed dose to water with a small standard uncertainty, a few requirements need to be fulfilled: As the radiation-induced temperature rise that is measured within the calorimetric experiment only amounts to about 0.24 mK/Gy [31], doses >1 Gy are usually applied [46] for a satisfying signal to noise ratio. In addition, the irradiated field for the calorimetric measurement of D_w should have a certain size as a very small field directly influences the heat conduction effects making greater corrections necessary and thereby also increasing their uncertainty [47, 18]. Heat conduction effects are also influenced by the time needed to irradiate the field, as the initially induced heat dissolves with time [47]. This means, a compromise has to made between irradiated dose and field size, and on the other hand irradiation duration. To determine the correction factors k_i, a detailed knowledge of the irradiation field is required. In order to achieve a low uncertainty in these factors, and thus a low uncertainty in the determined D_w, the irradiation field has to be reproducible and homogeneous [46]. The irradiation field parameter and criteria choosen for this work will be presented below (Chapter 3.1).
At the German national standard laboratory PTB, water calorimetry is used as the primary standard for the absorbed dose to water. Here, ICs are calibrated in the PTB's reference field (^{60}Co) by means of water calorimetry.

2.2.3 Practical dosimetry using calibrated ICs

In practical reference dosimetry, calibrated ICs are used. Therefore, the IC is brought into in a reference field with beam quality Q_0, for which the absorbed dose to water D_{w,Q_0} has been determined beforehand for reference conditions. Usually this reference field is a ^{60}Co beam [48]. Measuring the corrected IC reading M_{Q_0} under defined reference measurement conditions, the calibration factor for the beam quality Q_0 is given by

$$N_{D,w,Q_0} = D_{w,Q_0}/M_{Q_0}. \tag{20}$$

To be able to use this calibration factor for measurements at a given beam quality $Q \neq Q_0$, a correction factor k_{Q,Q_0} has to be introduced correcting for the difference in the IC's response to the beam qualities Q and Q_0. This factor is defined as the ratio of the calibration factors for both beam qualities:

$$k_{Q,Q_0} = \frac{N_{D,w,Q}}{N_{D,w,Q_0}} = \frac{D_{w,Q}/M_Q}{N_{D,w,Q_0}}. \tag{21}$$

k_{Q,Q_0} is a chamber-specific correction factor; for a known calibration factor N_{D,w,Q_0} of the IC used, it can be experimentally determined by measuring the absorbed dose to water $D_{w,Q}$ and the IC reading M_Q under the same irradiation conditions. For the corrected IC reading M_Q in the beam quality Q, the absorbed dose to water $D_{w,Q}$ is then given by

$$D_{w,Q} = M_Q \cdot N_{D,w,Q_0} \cdot k_{Q,Q_0}. \tag{22}$$

In the following k_{Q,Q_0} will be referred to as k_Q.

2.2.4 Current status of reference dosimetry in carbon-ion beams

Following international recommendations by the IAEA given in the International Code of Practice for the Dosimetry of External Radiotherapy Beams TRS-398 [10], k_Q is determined via theoretical calculations due to a lack of experimental data. Therefore, the following equation is given:

$$k_Q = \frac{(s_{w,air})_Q}{(s_{w,air})_{Q_0}} \frac{(W_{air})_Q}{(W_{air})_{Q_0}} \frac{p_Q}{p_{Q_0}}. \tag{23}$$

Hereby, $s_{w,air}$ is defined as the ratio of the mean restricted mass stopping powers of water and air, W_{air} denotes the mean energy spent to form an ion pair in air. p is the overall perturbation factor for the IC used, it can be calculated as the product of perturbation factors correcting for different effects:

- p_{cav}: The air cavity changing the electron fluence at the measurement position
- p_{cel}: The influence of the IC's central electrode on the irradiation field
- p_{wall}: The influence of the non-water-equivalent chamber wall

- p_{dis}: The effect of the replacement of water by the IC cavity when the IC's reference point is taken to be at the chamber centre

Due to a lack of experimental data, constant values are adopted for $(s_{w,air})_Q$ and $(W_{air})_Q$ which are valid for all ions with $2 \leq Z \leq 18$, assuming $(s_{w,air})_Q$ and $(W_{air})_Q$ to be independent of the beam quality and neglecting contributions of fragmentation processes. As no information on the perturbation effect of ICs in ion beams is available, p_Q is assumed to be unity. The stated corresponding relative standard uncertainties are 2.0 % for $(s_{w,air})_Q$, 1.5 % for $(W_{air})_Q$ and 1.0 % for p_Q. This results in a combined standard uncertainty of k_Q of 2.8 %. An updated version of the TRS-398 shall be published in 2021 [49].
German national standard regulations stated in the DIN 6801-1 [13] also prescribe calculated k_Q values for heavy ion beams according to Equation 23, but introducing the stopping power ratio $(s_{w,air})_Q$ as a function of the residual range R_{res} according to

$$s_{w,air} = a + b \cdot R_{res} + \frac{c}{R_{res}}, \tag{24}$$

for $R_{res} \geq 0.03\,\text{cm}$. Hereby, the residual range is defined as the difference between the measurement depth and the depth at which the value of the percentage depth dose distribution after the Bragg peak (100 %) has dropped to 50 %. For ions with $2 < Z \leq 10$, $a = 1.120$, $b = -3.998 \cdot 10^{-5}\,\text{cm}^{-1}$ and $c = 3.942 \cdot 10^{-4}\,\text{cm}$. A relative standard uncertainty of 1.5 % is stated for the resulting stopping power ratio, leading to a somewhat lower overall standard uncertainty of k_Q of 2.2 %. The values used for the calculation of k_Q according to TRS-398 and DIN 6801-1 using Equation 23 are summarized in Table 1.

Quantity	TRS-398	DIN 6801-1
$(s_{w,air})_Q$	1.130 (2.0 %)	1.120 (1.5 %)
$(s_{w,air})_{Q_0}$	1.133 (0.5 %)	1.122 (0.1 %)
$(W_{air})_Q$ / J/C	34.50 (1.5 %)	34.50 (1.5 %)
$(W_{air})_{Q_0}$ / J/C	33.97 (0.2 %)	33.97 (0.2 %)
p_Q	1.0 (1.0 %)	1.0 (1.0 %)
p_{Q_0}	Listed in table B.I. TRS-398 [10] (0.6 %)	TRS values multiplied by k_r (see Equation 25, 26) (0.6 %)

Table 1: Values for $s_{w,air}$, W_{air} and p for the beam qualities Q (ion beams with $2 \leq Z \leq 18$ for TRS-398 and $2 \leq Z \leq 10$ for DIN 6801-1) and Q_0 (^{60}Co) used for the theoretical calculation according to Equation 23 as stated in TRS-398 [10] and DIN 6801-1 [13]. The corresponding relative standard uncertainties are given in parentheses. $(s_{w,air})_Q$ according to DIN 6801-1 was calculated for a residual range of 3.29 cm (as given for the calorimetric measurement position, see Chapter 3.4) using Equation 24.

Chamber positioning In the beam quality Q, both TRS-398 and DIN 6801-1 prescribe a positioning of the chamber's reference point $0.75 \cdot r_{IC}$ deeper than the measurement position z to use the tabulated k_Q factors; hereby, r_{IC} denotes the chamber's radius. At beam quality Q_0, the reference point shall be positioned at z for the determination of

N_{D,w,Q_0}. In the TRS-398, this displacement effect is included as a factor p_{dis,Q_0} in the overall perturbation factor p_{Q_0} used for the theoretical calculation of k_Q (Equation 23), whereas the DIN 6801-1 introduces an additional IC-dependent factor k_r.
As the IC positioning as well as the treatment of the displacement effect as stated in TRS-398/DIN 6801-1 differs from the experimental situation during the water calorimetric measurements (see Chapter 3.5), the experimental factors k_Q will be expressed as k_Q^{TRS} and k_Q^{DIN} according to the definitions given in these reports as follows:

$$k_Q^{TRS} = k_Q \cdot (1 + 0.75 r_{IC} \cdot \delta_{^{12}C})^{-1} \tag{25}$$

$$k_Q^{DIN} = \frac{k_Q}{k_r} \cdot (1 + 0.75 r_{IC} \cdot \delta_{^{12}C})^{-1} \tag{26}$$

with $\delta_{^{12}C}$ denoting the relative depth dose gradient of the irradiation field at the measurement position. k_r is defined as $(1 - 0.003 \cdot r_{IC})^{-1}$ [13]; using the ICs' radii given in Table 4, this gives a value of $k_r = 1.009$ for both ICs used within this thesis. These values k_Q^{TRS} and k_Q^{DIN} can then be compared to the values stated in the literature.

3 Material and Methods

In this chapter the different devices, experimental setups and methods used within this thesis are presented.
The following chapters 3.1.2, 3.1.3, 3.1.4, 3.2 and 3.3 are based on article [1]; 3.2.1 is based on article [2]. Chapters 3.4, 3.5 and 3.6 are based on article [3].

3.1 Irradiation

All measurements were performed at the Heidelberg Ion-beam Therapy Center (HIT). The beam delivery system at HIT as well as the irradiation methods used within this work, such as the irradiation plan and the 2DRM for a passive modulation of the SOBP, are presented in this chapter.

3.1.1 Beam delivery system at HIT

The Heidelberg Ion-beam Therapy Center (HIT) as a part of the Heidelberg University Hospital has been in clinical operation since 2009 [50]. It has three treatment rooms, two of which with a horizontal beam line and one with a gantry allowing to rotate the ion source by 360° around the patient, as well as one experimental room for quality assurance (QA) measurements and pre-clinical studies. All experiments within this thesis were performed at this "QA-room".
The acceleration takes place, in a first step, using a linear accelerator (LINAC) before the ions are being injected into a synchrotron, where a final beam energy of up to 430 MeV/u can be reached. The ions available at HIT are protons, helium, carbon and oxygen, whereby only protons and carbon ions are clinically used at the moment. As the maximum number of particles per synchrotron cycle is limited, the final beam has a pulsed structure with beam-on times of about 5 s and beam-off times of about 4.5 s, where new particles are accelerated to the requested energy. The maximum beam intensity available at HIT (defined as the number of particles per synchrotron cycle) is $1 \cdot 10^9$ for carbon ions [51].
The beam is actively delivered using the so-called intensity-controlled rasterscan technique based on the developments at GSI [52]: A focused beam is scanned point by point over the target volume by means of vertical and horizontal magnets in the x- and y-directions; by actively adapting the beam's energy, different slices in depth (z-direction) are scanned. This technique allows an optimal target coverage. The beam's focus width is defined as the full width at half maximum (FWHM) of the Gaussian distribution that is assumed for both the horizontal and vertical beam profiles; it ranges from 4 - 20 mm in air at the isocenter [51].
The beam delivery is controlled by the beam application monitoring system (BAMS) developed by SIEMENS AG; it is located in the beam nozzle at each irradiation room. It consists of three identical ICs detecting the number of particles delivered per irradiation spot, sandwiched by two multi-wire proportional chambers (MWPCs) for the detection of the beam's horizontal and vertical position. The time-resolved measurement data of the

ICs and the MWPCs including the beam position and width in the x- and y-directions, the number of delivered particles per spot and the irradiation duration is being stored in the so-called machine beam records.

For all irradiations, a 3 mm ripple filter was used. It consists of a PMMA plate with a periodic structure of fine grooves [53] and is located inside the beam nozzle. The ripple filter broadens the Bragg Peak and thereby smooths the resulting dose distribution.

3.1.2 Requirements for the irradiation

For the water calorimetric determination of the absorbed dose to water, a homogeneous irradiation field of a reasonably size and dose irradiated in a short time is needed. The following parameters were defined for this purpose, as they were also specified in [1]:

A dose of 1.5 Gy should be applied for a reliable signal to noise ratio. A field size of $6 \times 6\,\mathrm{cm}^2$ was choosen which fully covers the sensitive parts of the calorimetric detector as well as the ICs used. The SOBP should have a depth of 6 cm resulting in a dose cube of $6 \times 6 \times 6\,\mathrm{cm}^3$. This field size was considered to be a good compromise with respect to the irradiation time (see below): A large field (as e.g. the reference field size of $10 \times 10\,\mathrm{cm}^2$ according to TRS-398 [10]) would require a long irradiation time, whereas a very small field would influence the heat conduction effects [47, 18].

Water calorimetric measurements are rather time-critical as the heat conduction corrections are especially dependent on the duration of the irradiation. Here, an irradiation time of less than 100 s should be achieved based on the findings by Medin *et al.* [20], who performed water calorimetric measurements in proton beams with an irradiation time of 2 min, and Osinga *et al.* [30], who irradiated a mono-energetic carbon ion field within about 95 s for water calorimetric measurements in the entrance channel of a mono-energetic carbon-on beam.

A passive modulation of the SOBP in terms of depth was needed, as a full three-dimensional active scanning of the irradiation field, as is usually done in carbon-ion therapy [51, 7] would take several minutes (about 8 min for a $6 \times 6 \times 6\,\mathrm{cm}^3$ volume of 1.5 Gy). Therefore, a static 2D range modulator (2DRM) [54] comparable to a ridge filter [55] was used. It is described in Chapter 3.1.3.

A detailed knowledge of the irradiation field is needed to determine correction factors for the water calorimetric (Chapter 3.4.2) and ionometric measurements (Chapter 3.5.2). For a low uncertainty in these factors, the field has to be reproducible and homogeneous [46]. As a criteria for homogeneity, the standard deviation of dose values within a sphere with 20 mm radius was calculated; the deviation of repeated measured values within this sphere was considered as a measure for the reproducebility. They should be below below 2 % for the homogeneity and below 0.5 % for the reproducebility, based on the findings by Osinga *et al.* [30]. The 20 mm radius was choosen to generously cover the position of the thermistor probes inside the calorimetric detector (see Chapter 3.4.1) and the ICs' volume (Chapter 3.5.1).

3.1.3 2D range modulator

Due to time restrictions during the water calorimetric measurements, the SOBP is passively modulated in depth using a so-called 2D range modulator (2DRM) [54, 56]. The 2DRM consists of many pyramid-shaped pins of the same height (as can be seen in Figure 2). When the 2DRM is positioned in the beam path, nearly mono-energetic particles pass through different thicknesses of the 2DRM's material depending on the position at which they hit one of the pins. This leads to an energy broadening of the beam creating Bragg peaks with different ranges, which superimpose to a SOBP. The resulting dose distribution in depth $D(z)$ can be described by the following equation:

$$D(z) = \sum_{i=1}^{N} w_i \cdot B(z + \Delta z \cdot i), \tag{27}$$

with $B(z)$ the pristine Bragg peak's depth dose distribution, Δz the step size between successive Bragg peaks and w_i the weight of the contribution of each Brag peak i to the resulting SOBP dose distribution $D(z)$. By optimizing the Bragg peaks' weights w_i, a homogeneous SOBP can be created. These optimized weights determine the well-defined profile of the 2DRM's pins which shows different gradients at different heights, as described by Simeonov *et al.* [54].

The 2DRM has a total area of 10 x 10 cm^2 to fully cover the irradiation field; each pin has a height of 57 mm. As a dose cube with constant dose was required for the water calorimetric measurements, the pin's shape and thereby also the created depth dose distribution is constant over the modulator's lateral area. Different pin base areas (period of the pin distance) of 2 x 2 mm^2, 3 x 3 mm^2 and 4 x 4 mm^2 were considered; their impact on the resulting irradiation field was tested. In addition, two identical 2DRMs were compared to investigate the reproducibility of the manufacturing process. The 2DRMs were produced using rapid prototyping with a Stratasys Objet30 Pro PolyJet 3D printer and the printing material RIGUR RGD450, a manufacturer's own polymer for which the composition is not specified. A schematic drawing of a 2DRM with 3 x 3 mm^2 pin base area is shown in Figure 2.

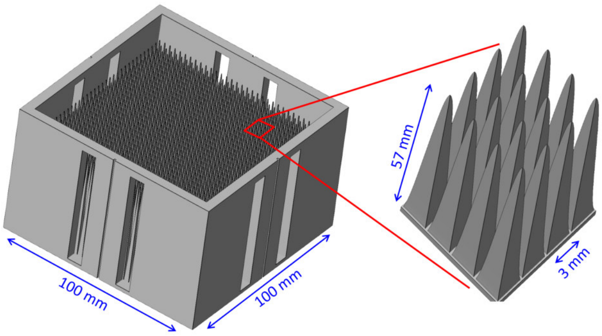

Figure 2: Schematic drawing of the 2DRM with 3 x 3 mm^2 pin base area with a detailed view of 4 x 4 pins. Reprinted from [1].

Positioning table The 2DRMs were placed on a positioning table to be able to investigate the impact of its positioning accuracy on the resulting dose distribution. This table allows a relative positioning accuracy of 5 μm in the x- and y-directions and 1 μm in the z-direction, as well as a defined tilting around each spatial axes: 0.1 ° around the x- and y-axes, less than 0.006 ° around the z-axis. The 2DRM was aligned using the wall-mounted laser system which offers a positioning accuracy of 0.5 mm [57]. In this way, a total alignment accuracy of the 2DRM of 0.5 mm in each direction and less than 0.3 ° around each spatial axes can be achieved.
The 2DRM was fixed in a 3D-printed holder which was attached to the positioning table for a stable position. The setup can be seen in Figure 3.

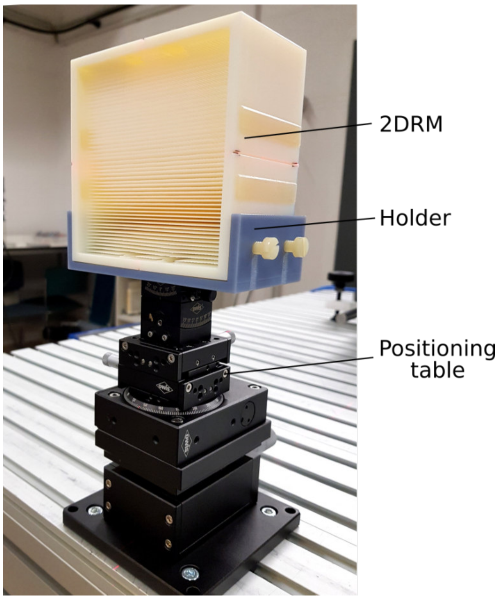

Figure 3: The 2DRM on the positioning table.

The back of the 2DRM was positioned at the isocenter for all measurements, the pins were pointing towards the beam nozzle.

3.1.4 Irradiation plan

As the SOBP was passively modulated in depth, only one energy was needed. This energy was defined by the maximum depth (that means the distal edge of the SOBP) inside the experimental setup that should be reached. As the calorimetric measurement position should be at 10 cm water depth inside the water calorimeter (which corresponds to a WET from the isocenter of 11.1 cm) and in the middle of the 6 cm wide SOBP, an energy of 278.29 MeV/u had to be choosen. The different layers inside the beam path, that lead to the given WET are summarized in Table 2 and are shown in Figure 11.

Material	geom. thickness / mm	WET / mm
Air	655.0	0.7
Polystyrene	202.5	6.5
Air	7.0	0.01
PMMA	3.0	3.5
Water (RW-3)	79.3 (77.3)	79.3 (79.2)
Glass	0.7	1.28
Water (RW-3)	20.1 (19.6)	20.1 (20.1)
$\sum$		**111.3**

Table 2: The different material layers in the beam path of the water calorimeter and, in parentheses, of the calorimeter slab phantom (mimicking the water calorimeter in the Peakfinder experiment, see Chapter 3.2.3) with its geometrical thicknesses and corresponding WETs. In summary, the WET from the isocenter to the measurement position at 10 cm water depth inside the calorimeter is given.

The best results concerning field homogeneity were achieved for a fourfold repainting of the irradiation field with the irradiated layers slightly shifted against each other. Therefore, the whole irradiation plan consisted of four layers of the same energy (278.29 MeV/u); each layer had 36 x 36 spots, a focus size of 8.2 mm FWHM and a spot distance of 2 mm, resulting in a 6 x 6 cm^2 field. The second, third and fourth layer were shifted against the first layer by 1 mm in the x-, y- and xy-directing. The scheme of the whole irradiation is shown in Figure 4.

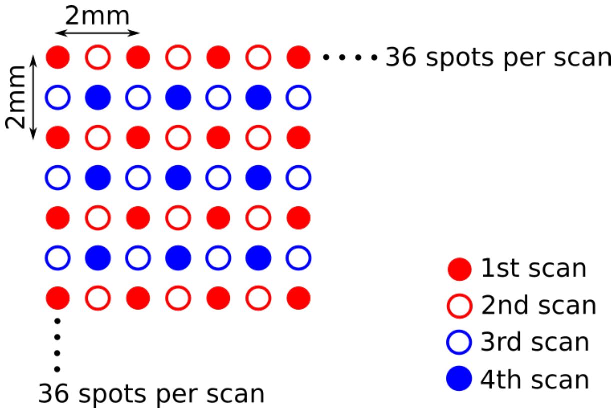

Figure 4: Scheme of the irradiation plan showing the four different layers that are irradiated in a sequence. Each layer consisted of 36 x 36 spots with a spot distance of 2 mm, they were shifted against each other by 1 mm. All layers were irradiated with the same energy of 278.29 MeV/u. Reprinted from [1].

A total dose of 1.5 Gy was irradiated following this scheme. For a short irradiation time, the highest clinically used beam intensity of $8 \cdot 10^7$ ions per second was choosen resulting in an overall irradiation time of about 90 s. This plan will be referred to the “standard irradiation plan”.

3.2 Field characterization

Field characterization measurements were performed (I) to find the best irradiation conditions (irradiation plan: focus, repainting, etc.) and 2DRM properties (pin base area, pin length), (II) to verify if the resulting field is suitable for water calorimetric measurements in terms of homogeneity and reproducebility, and (III) to be able to determine correction factors for the calorimetric and ionometric measurements based on the dose distribution.

3.2.1 2D field homogeneity: Film measurements

Film measurements were performed to analyse the pattern in the irradiation field induced by the 2DRM, as film provides a very high spatial resolution. In addition, it should be verified experimentally if the spatial resolution of the IC array Octavius 1000p is sufficient for the detailed characterization of the irradiation field (as presented in Chapter 3.2.2). To this purpose, self-developing radiochromatic film (Gafchromic®EBT3, lot number 10031801) was used as it is also widely employed in clinical routine [58].

EBT3 film consists of an active 28 μm layer between two 125 μm matte-polyester layers [59]. When exposed to radiation, the active layer becomes polymerized, changing the light absorption properties in the irradiated film region. The film is self-developing, e.g. no developing process is needed [60]. After a certain development time after the irradiation, it is read out using a flatbed scanner. EBT3 film has a high spatial resolution of max. 25 μm (the spatial resolution of the measurement may be lower depending on the performance of the read-out system) and is nearly equivalent to tissue [61].

Film measurements can be affected by artifacts and material inhomogeneities [62, 63], variations in the active layer may add variation to the film signal and by that also to the measured dose. A well-established method to reduce these artifacts is the triple channel analysis method. Here, the information from all three color channels is used to separate the dose-independent part of the signal from the resulting dose distribution. Micke *et al.* [64] and Mayer *et al.* [65] introduced different approaches to this multichannel method, generating identical resulting dose distributions. Other channel-independent correction methods such as the weighted mean model and the truncated normal distribution model were presented by Méndez *et al.* [66, 67]. The application of these methods has been investigated in photon radiotherapy [68, 69, 70] as well as in brachytherapy [71]. Within this thesis, it was applied for carbon-ion irradiated film for the first time.

The dosimetric properties of EBT3 in carbon-ion beams investigated e.g. in [72] showed a signal dependency on the ionization density. For mono-energetic beams, a decreased response of EBT to carbon ions of about 30 % compared to photons was observed [73]. A quenching effect appeared that increased with depth [74]. It was shown that the film response is dependent on the ion type and its energy, which means that in carbon-ion beams, due to the nuclear fragmentation process, the optical density is not uniquely connected to the dose for most cases. Nevertheless, it is possible to use EBT film in carbon-ion beams if restricted to relative dose measurements of lateral distributions with similar ionization density, as it was the case for the measurements performed here.

Scanning The film specimens were scanned at least 32 h after the irradiation, as a 24 h post-exposure time is recommended, preferably 48 h [75]. An Epson Expression 10000XL flatbed scanner was used. First, 10 pre-scans of the entire scanning field were performed to ensure a constant working temperature [76, 77]. Then, the film specimens were scanned as positive film in transparency mode. Every specimen was scanned separately, positioned at the middle of the scanning field to minimize lateral scan artifacts [78]. Care was taken to position every specimen in the same orientation on the scanner relative to its position during the irradiation. The specimens were kept flat on the scan field using a glass compression plate [79]. They were scanned with resolution of 72 dpi and 48-bit color depth, all color-correction features were deactivated. Each specimen was scanned once, since the investigated reproducibility of scanning was found to be 0.1 % of the maximum. Each scanned image was separated into its red, green and blue color component using the *convert* tool from the software *ImageMagick* [80]. From the pixel values P, the optical density OD for each pixel was calculated using

$$OD = log_{10} \frac{P_{blank}}{P}, \tag{28}$$

with $P_{blank} = 65325$ taken from a flood field image (nothing was placed on the scanner).

Calibration A calibration curve was determined to be able to obtain a dose-related quantity from the optical density. Therefore, eight single fields of different number of primary particles in the range of (0.05 - 1.5) $\cdot 10^{-6}$ mm^{-2} corresponding to absorbed doses to water between 0.1 and 3.2 Gy (measured with a calibrated IC) were irradiated onto one EBT3 film specimen at a water-equivalent depth of 2.9 mm. The beam had an initial energy of 278.29 MeV/u, as it was also used for all other measurements.
In addition to the carbon-ion irradiation calibration curve, film specimens were also irradiated at a 6 MV LINAC (Elekta Synergy) to compare the resulting calibration curves. Here, doses in the range of 0.5 - 3.0 Gy (determined from the LINAC's monitor units) were irradiated; the specimens were positioned at 10 cm depth in a water-equivalent slab phantom.
For each calibration field the mean optical density for a central ROI of 56 x 56 px was determined and plotted against the corresponding irradiated dose. Equation 29 was fitted to this plot, yielding the fitting parameters a, b and c for each color channel.

$$D(OD) = \frac{c \cdot 10^{-OD} - a}{b - 10^{-OD}}, \tag{29}$$

Triple channel analysis In order to reduce film artifacts and make the measured dose distribution better visible, the triple channel analysis according to Micke *et al.* [64] was applied. This analysis method separates the non-dose-related part of the film signal which is caused by film or scanning artifacts, from the dose-related part. To this end, a disturbance value δ is introduced, it describes the dose-independent disturbance in the measured optical density. The dose D_X for the color channel X using the corresponding calibration function f_X (Equation 29) is then given by

$$D_X = f_X(OD_X \cdot \delta), . \tag{30}$$

It is important to notice that the calibration condition for the average disturbance $\overline{\delta} = 1$ is fulfilled; this is the case for a sufficiently large measurement area reflecting average response of the system [64]. δ was determined by minimizing the differences between the doses values of the three color channel red, green and blue for each pixel according to the following equation:

$$\Omega(\delta) = min\left(\sum_{i \neq j}(D_{X_i} - D_{X_j})^2\right), \tag{31}$$

with $X_i, X_j \in \{R, G, B\}$ denoting the three color channels red, green and blue. To avoid diverging calculations due to artifacts in the scans, the constraint $0.8 \leq \delta \leq 1.2$ was set for the minimization [81]. The optical density obtained from the film was greatest for the red color channel [60], as the main absorption band is at 633 nm [82]. Therefore, the corrected dose distribution was calculated by multiplying the optical density from the red channel by the value obtained for δ.
The data was processed by means of a Python routine using the NumPy package [83] and the Image module from the Pillow package [84]; equation (31) was solved by means of the minimizer routine from SciPy [85].

Gamma index analysis A gamma index analysis was performed as described by Low *et al.* [86] to compare the dose distributions measured with EBT3 film (and corrected by the triple channel analysis) and the IC array (see chapter 3.2.2). Thereby, the IC array's spatial resolution should be checked.
The gamma index analysis yields a numerical quality index for the comparison of two dose distributions (here referred to as distribution 1 and 2). As a criterion, it combines the distance to agreement (DTA) as the smallest distance between two points of the distributions to be compared that show the same dose, and a dose-difference criterion. A measured point $\overrightarrow{r_1}$ of distribution 1 with dose $D_1(\overrightarrow{r_1})$ is compared to a measurement point $\overrightarrow{r_2}$ of distribution 2 with dose $D_1(\overrightarrow{r_1})$ by the value Γ using the defined distance criterion Δd and dose criterion ΔD:

$$\Gamma(\overrightarrow{r_1}, \overrightarrow{r_2}) = \sqrt{\frac{r^2}{\Delta d^2} + \frac{\delta^2}{\Delta D^2}}, \tag{32}$$

with the distance between the two points $r = |\overrightarrow{r_1} - \overrightarrow{r_2}|$ and the dose difference $\delta = D_1(\overrightarrow{r_1}) - D_2(\overrightarrow{r_2})$. Based on this, the gamma index γ is defined as

$$\gamma = \min\{\Gamma(\overrightarrow{r_1}, \overrightarrow{r_2})\} \, \forall \overrightarrow{r_2}. \tag{33}$$

If $\gamma \leq 1$, the measured point $\overrightarrow{r_1}$ passes the analysis, otherwise the defined threshold is exceeded and the analysis fails. This calculation is repeated for all measurement points of dose distribution 1.

3.2.2 2D dose measurements: IC array

The IC array PTW Octavius 1000p was used to measure 2D dose distributions. It consists of 977 ICs arranged in an 11 x 11 cm^2 rectangle with a distance of 2.5 mm in the inner 5 x 5 cm^2 and 5 mm in the outer part of the detecting area, as it can be seen in Figure 5. Each IC has an active area of 2.3 x 2.3 mm^2 [87]. The 1000p is adapted for particle-beam applications with the ICs filled with air instead of liquid to avoid recombination effects.

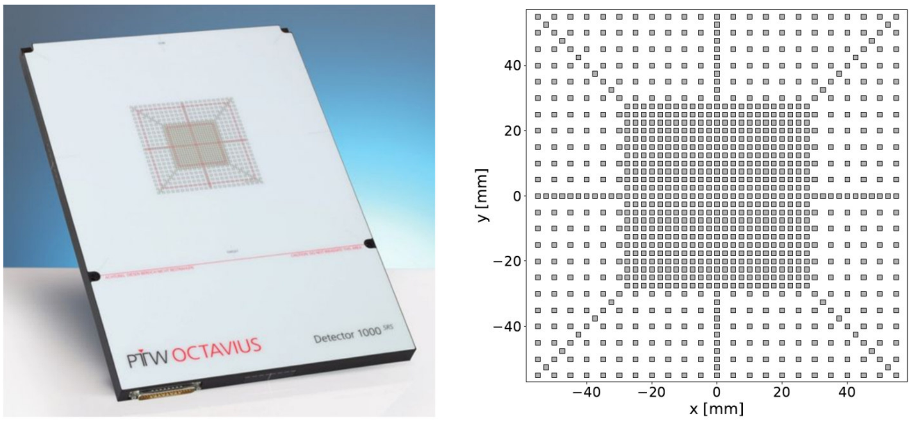

Figure 5: Picture of the PTW Octavius 1000p (left) [88] and schematic drawing of the ICs' arrangement (right) [87].

The IC array was only used for relative dose measurements. The dose distributions were normalized to the mean of the dose values within a 20 mm radius around the center. In this way, the measurements could be better compared.

Calibration of the relative response The IC array was calibrated for the chamber's response relative to each other at a well characterized 6 MV photon field at PTB Braunschweig. Measurements were performed with the array at a measurement depth inside a slab phantom corresponding to 10 cm depth in water; different doses between 0.5 and 5.0 Gy were irradiated. The irradiation field was characterized beforehand using a calibrated Pinpoint IC scanned across the field.

Water phantom setup The IC array was positioned in a water phantom inside a waterproof PMMA case. The upper edge of the case is attached to a linear drive at one side and to a smooth-running rail at the other side. Thus, the IC array can be moved remote-controlled in depth inside the water phantom with a positioning accuracy of 0.1 mm, allowing a three-dimensional measurement of the dose distribution. This setup was developed for the purpose of a fast and effective characterization of the irradiation field around the water calorimeter's measurement position. Therefore, it is placed on the same earth anchors mounted to the floor of the QA-room as the water calorimeter (see Chapter 3.4.1) assuring a reproducible position. The setup is shown in Figure 6. The phantom was built at the PTB workshop and is similar to the setup developed by

Schuy *et al.* [89].

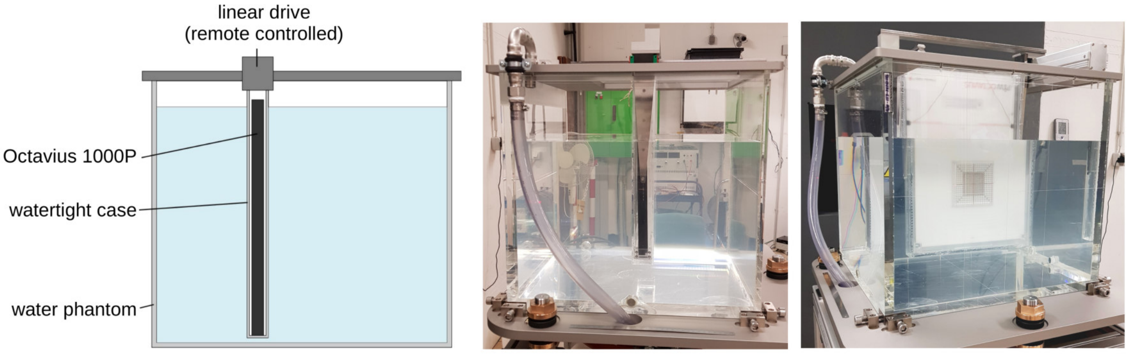

Figure 6: Schematic drawing of the water phantom setup in side view (left); side view (middle) and front view (right) of the setup with IC array positioned inside the PMMA case and the water phantom filled with water. Reprinted from [1].

For the repeated field characterization measurements, the IC array was moved in steps of 2.5 mm in depth over a course of 85 mm covering the whole SOBP including parts of the entrance channel and the fragmentation tail. A polysterol block of the same thickness and material as the calorimeter's insulation was positioned in front of the phantom to better map the irradiation conditions inside the calorimeter.

To compare the depth dose distributions measured with this setup with the Peakfinder data, the Octavius' measured values within a radius of 41 mm around the center (corresponding to the active area of the Peakfinder's measurement chamber) were averaged for each depth. For the coordinates in depth (z-axis), the measurement position relative to the isocenter, the phantom's and the array case's PMMA wall thicknesses, the linear drive's offset and the Octavius' measurement depth, in total 51 mm, were taken into account.

As a quantity for field homogeneity, the relative standard deviation of measured dose values within a sphere with 20 mm radius around the center of the dose cube was calculated. Repeated field characterization measurements were performed to investigate the reproducebility of the distribution. For each measurement point, the standard deviation of the repeated measurements was calculated; the mean of these standard deviations was then taken as the measure of reproducibility.

Data interpolation For the graphical visualization and comparison of the dose distribution as well as for the determination of correction factors such as k_l (Chapter 3.4.2) and k_v (Chapter 3.5.2), the Octavius' discrete measurement points were one-dimensionally interpolated according to the Nyquist–Shannon sampling theorem [90], using a Python routine as also done by Bauer [87]. First, the 1D-measurement data was multiplied by a Tukey window function (from the SciPy package [85]) of the same dimensions in order to smoothly level down the data to zero at its outer edges. This prevented oscillating artifacts in the interpolated data. The Tukey window function, also called cosine taper window, is defined as

$$w(n) = \begin{cases} 1 & \text{for } 0 \leq n \leq \alpha \frac{N}{2} \\ \frac{1}{2} \cdot \left(1 + \cos \pi \left[\frac{n - \alpha(N/2)}{(1-\alpha)(N/2)}\right]\right) & \text{for } \alpha \frac{N}{2} < n \leq \frac{N}{2} \end{cases} \tag{34}$$

for N total points and α defining the window's plateau width [91] as shown in figure 7. The plateau width had to be choosen carefully: If the plateau is too wide, oscillating artifacts in the interpolated data are not completely suppressed due to the steep slopes on both sides of the plateau. On the other hand, a narrower plateau means an even greater loss of data, since a larger portion of the measured values is changed by the window function. Here, an α value of 0.3 was found to be a good compromise.

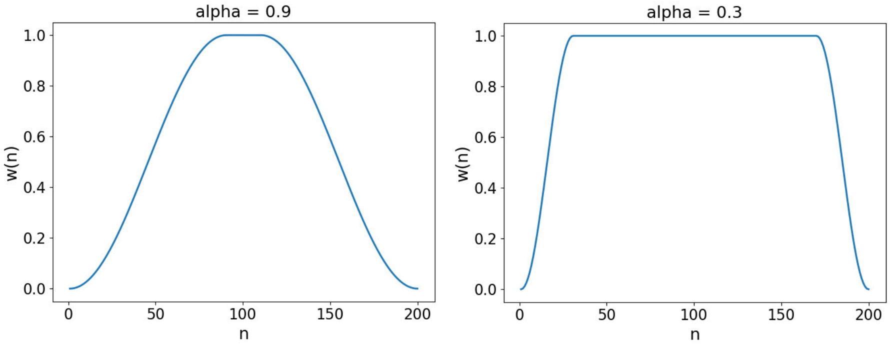

Figure 7: Tukey window function for $\alpha = 0.9$ (left) and $\alpha = 0.3$ (left) as it was applied for the interpolation of the Octavius 1D-measurement data.

Next, a one-dimensional discrete Fourier transformation was performed to the data using the *fft.fft* function from the Python NumPy package [83]. After adding 200 zeros to both sides of the Fourier transform, the data was transferred back performing an inverse Fourier transformation using the *fft.ifft* function. This added points between the actual measurement points, resulting in a smooth curve connecting the discrete points.

3.2.3 Depth-dose measurements

The PTW Peakfinder Water Column [92] was used to measure the depth dose distributions of the different 2DRM models. It consists of a reference detector (plane-parallel Bragg peak type 34082 chamber) fixed at the entrance window and one measuring detector (type 34080 chamber) between two water-containing bellows that are adjustable in length. In this way, the measuring detector can be moved in depth, measuring depth dose distributions with a spatial resolution of 10 μm and a positioning accuracy of 100 μm. Its movement is synchronized with the synchrotron's spill signal. The measuring detector has a circular sensitive area with a 41 mm radius. Both chambers were operated at 400 V using a PTW-TANDEM XDR dual channel electrometer.

Due to spatial constrains inside the QA-room, the Peakfinder's front window was positioned at the isocenter for all Peakfinder measurements. The 2DRM was positioned

65.5 cm in front of it, as this is also the distance between 2DRM and water calorimeter (see Chapter 3.4). The setup is shown in Figure 8. The Peakfinder's offset of 19.5 mm was taken into account for all measurements.

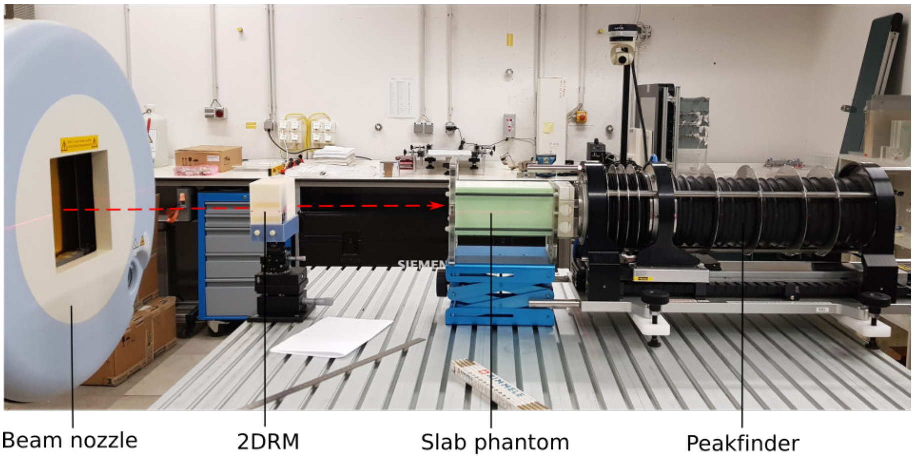

Figure 8: Experimental setup of the Peakfinder measurement with the beam nozzle (left), the 2DRM on the positioning table and the calorimeter slab phantom in front of the Peakfinder (right). The dashed red line indicates the beam path.

Calorimeter slab phantom The slab phantom positioned in front of the Peakfinder mimes the water calorimeter in terms of absorption and scattering. It consists of slabs of the same materials and thicknesses as they are in the beam path for the water calorimetric measurements, except for the water which is replaced by solid water (RW-3, PTW, Germany) slabs of corresponding thickness. Thicknesses and materials of the slabs are listed in Table 2. The phantom was a modified version of the one used by Osinga *et al.* [30]; additional RW-3 slabs were added to reach a measurement depth of 10 cm in water whereas Osinga *et al.* used the phantom for a maximum depth of 5 cm.

3.2.4 IC measurements at the isocenter

Repeated measurements with an IC (PTW TM30013, see Chapter 3.5.1) were performed over a period of 16 months, irradiating the standard irradiation plan without the 2DRM. The IC was positioned inside a solid water slab phantom (RW-3, PTW, Germany) with its reference point at the isocenter. With this measurements, the time stability of the delivered dose independent from the positioning of the 2DRM was examined. The determined variation in the delivered dose was considered in the overall uncertainty budget of k_Q.

3.3 Monte Carlo simulations

Monte Carlo (MC) simulations were performed to analyse the particle spectra at the measurement position. Thereby, it should be investigated if the resulting k_Q values for the passively modulated SOBP can be transferred to active scanning conditions, as an active beam scanning is prevalent in clinical carbon-ion radiotherapy [7]. Different scattering processes due to different material in the beam path and different initial beam energies may lead to the beam qualities for passively modulated and actively scanned SOBP differing. This was examined by comparing the particle and LET spectra defining the beam quality at the calorimetric measurement position of both irradiation modalities. All MC simulations were performed using the FLUKA transport code version 2011.2x.5 [93]. The settings are described below.

3.3.1 FLUKA transport code

The settings for precise simulations (PRECISIO) were used for all simulations. For the passively modulated SOBP, a 278.29 MeV/u carbon-ion beam was simulated with a rectangular beam shape and an area of 11 x 11 mm^2 to fully cover the area of the 2DRM implemented (see Chapter 3.3.2). The actively scanned irradiation field consisted of 22 layers with energies ranging from 196.23 MeV/u to 272.77 MeV/u to create a 6 cm SOBP comparable to the 2DRM-modulated SOBP.

The full experimental setup was implemented including the 3 mm ripple filter and the different layers of the calorimeter. The BAMS was not taken into account for the simulation, as its WET was already considered in the Peakfinder's offset; thus, the depth dose distributions resulting from the Peakfinder experiment and the simulation could be compared as a proof of concept for the simulation setup. The ripple filter was modeled using several rectangular parallelepipeds and infinite half-spaces crossing the parallelepipeds, its material was set to water. The calorimeter was implemented as rectangular material slabs imitating the different calorimeter materials in the beam path. The entire setup is shown in Figure 9.

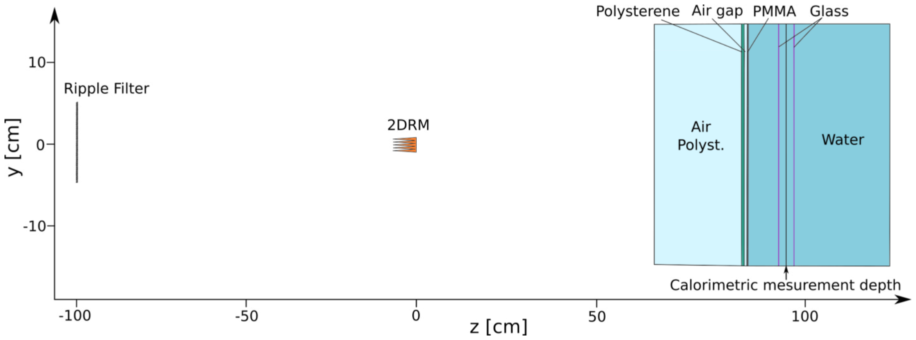

Figure 9: Measurement setup as it was implemented in the MC simulations. z-coordinates indicate geometrical depths. Reprinted from [1].

3.3.2 Implementation of the 2DRM

Due to its complex structure, the 2DRM was implemented in the simulation as a voxel geometry. As this is limited within the FLUKA code, only a section of 5 x 5 pins could be realized. Each pin had a 3 x 3 mm^2 base area and a 57 mm height.
For the implementation as a voxel geometry, the STL-file (data file containing the geometric information for 3D printing) of a single pin was converted into a text file which contained the voxel coordinates using an online voxelizer program [94]. After reshaping and duplicating the single pin to a 5 x 5 pins geometry, the voxel text file was converted into a FLUKA voxel geometry file using the FORTRAN routine *writegolem* [93]. This file was implemented in FLUKA using the VOXELS card. As the exact composition of the 3D printing material was not given by the manufacturer, the voxel's material was set to water and the voxel's size was scaled with the water-equivalent thickness (WET) of the 2DRM's material. The WET was experimentally determined using the Peakfinder as described in Chapter 2.1. Different resolutions of the voxel geometry ranging from 59 x 59 x 56 voxel per pin (vx/pin) to 160 x 160 x 152 vx/pin were tested.

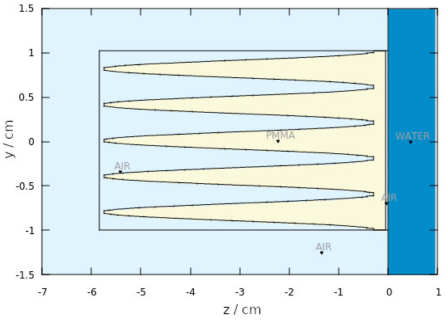

Figure 10: Side view of the 2DRM as it was implemented in FLUKA as a voxel geometry of 5 x 5 pins.

3.3.3 Scoring

The absorbed dose to matter was detected using the USRBIN DOSE card. The fluence, fluence-weighted LET and dose-weighted LET were recorded using the USRBIN ALL-PART card and an additional FORTRAN routine implemented in the FLUKA simulation. For each quantity, the particle spectra for particles with atomic number $Z = 1 \ldots 6$ were determined using the AUXSCORE card. Each USRBIN detector had a size of 5 x 5 x 20 cm^3 (x y z), with one detecting bin in the x- and y-directions and 400 bins in the z-direction to record distributions in depth.

3.4 Calorimetric measurements

The absorbed dose to water was determined by means of water calorimetry via Equation 19, measuring the radiation-induced rise in temperature inside an insulated water phantom. The measurement position was in the middle of the SOBP at 10 cm depth in water inside the calorimeter corresponding to a WET from the isocenter of 11.1 cm. In total, four calorimetric measurement campaigns were performed over a time period of 18 months, each consisting of one night shift for field characterization measurements (see Chapter 3.2.2) to ensure a stable dose distribution, followed by two night shifts of water calorimetric measurements and one night shift of ionometric measurements (see Chapter 3.5). Within each campaign, 65-88 calorimetric measurements were done.

3.4.1 The PTB water calorimeter

The calorimetric measurements were performed using the PTB portable water calorimeter designed for horizontal beams; it was operated at a water temperature of 4°C [15]. The calorimeter consists of a cubic water phantom with an edge length of 30 cm which is thermally insulated against the room temperature. The insulation consists of actively cooled aluminum plates sandwiched by two 5 cm thick layers of Styrofoam, surrounding the whole water phantom except for the entrance window. Here, a 20 cm thick Styrofoam block is used as insulation. Cooling channels connected to an external cooling unit lead cooling liquid through the aluminum plates. To accelerate the cooling from room temperature to the operating temperature at 4°C, the liquid can be additionally lead through a stainless steel tube inside the water phantom. This tube is closed several hours before and during the calorimetric measurements to reach and maintain a thermal equilibrium. A mechanical stirrer is located on the bottom of the water phantom which is used after one block if irradiations (see Figure 15) to homogenise the temperature distribution again.

The water calorimeter was positioned on earth anchors mounted to the floor of the QA-room 65.5 cm behind the isocenter. This allowed a stable and reproducible measurement position. The 2DRM was positioned in front of the calorimeter with its back in the isocenter. The detailed structure of the calorimeter including the different material layers in the beam path as also given in Table 2, is shown in Figure 11; the entire setup at the QA-room can be seen in Figure 12.

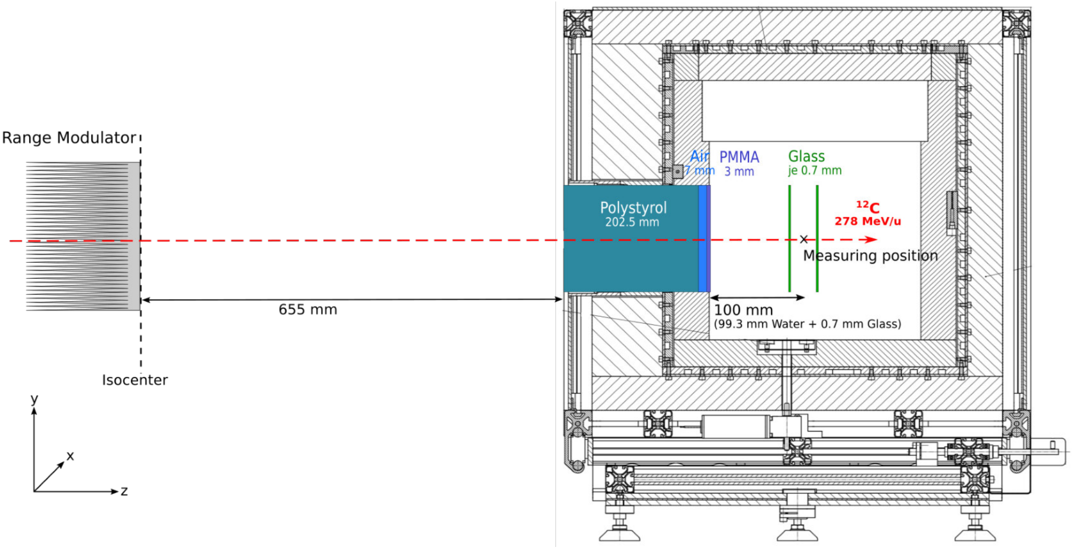

Figure 11: Water calorimetric measurement setup with the 2DRM positioned in the isocenter and the PTB portable water calorimeter 65.5 cm behind (sizes are not true to scale). The different material layers of the water calorimeter in the beam path are shown in detail. The dashed red line indicates the beam path. Reprinted from [3].

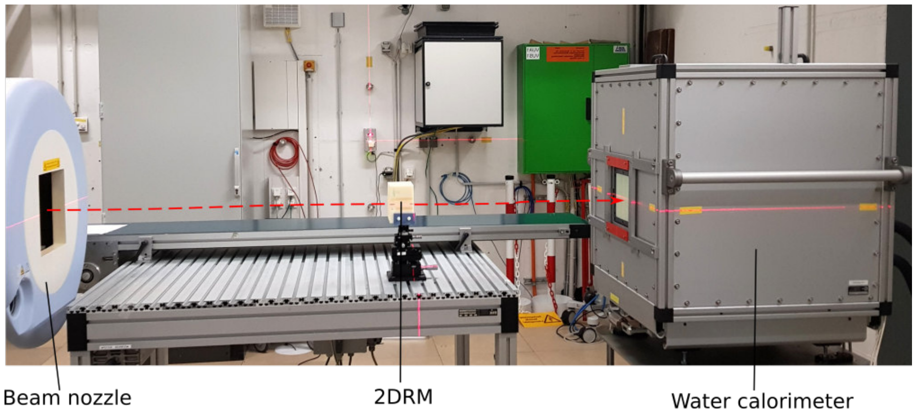

Figure 12: Picture of the calorimetric measurement setup with the beam nozzle (left), the 2DRM on the positioning table (middle) and the water calorimeter (right). The dashed red line indicates the beam path.

Calorimetric detector The calorimetric detector that was positioned inside the calorimeter consists of a thin-walled plane-parallel glass cylinder with 95 mm outer diameter and 41.4 mm outside length. The flat walls have a thickness of 0.70 mm, the cylinder walls' thickness is 2.5 mm [15]. The cylinder is filled with purified water, which is saturated with hydrogen and was pre-irradiated with about 50 Gy dose in order to assure a zero heat defect (see Chapter 3.4.2).
As the detecting elements, two thermistors fused into glass pipettes are mounted inside the cylinder perpendicular to the cylinder axis. They are opposite each other with a distance to the beam axis of about 3.5 mm (exact values are given in Table 3). The glass pipettes are conically shaped with an outer diameter between 0.51 mm and 0.61 mm at the end sections (varying between different detectors). The detector is shown in Figure 13.

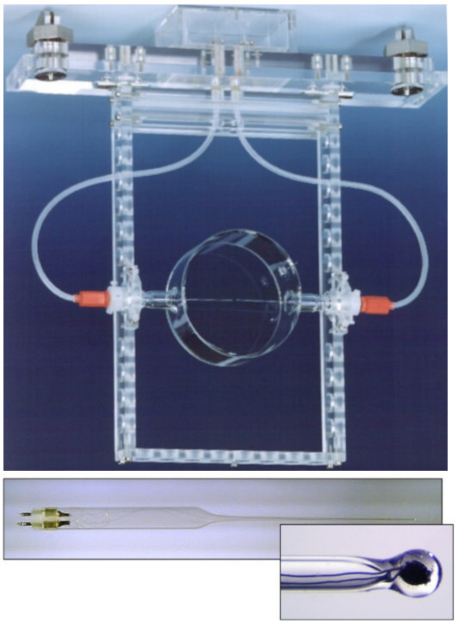

Figure 13: Upper Picture: Water calorimetric detector consisting of the water-filled glass cylinder held in a PMMA frame and the thermistor probes fused into glass pipettes that are placed in the cylinder from both sides. Lower pictures: One glass pipette as it is positioned inside the glass cylinder and detailed view of the pipette's tip with the thermistor fused into it. Reprinted from [31].

The calorimetric detector can be mounted at different depths in water relative to the entrance window with the central beam axis matching the cylinder axis. Within this thesis, a geometrical measurement depth of about 10 cm relative to the inner water phantom's wall (beam entrance window) was used which corresponds to the middle of the SOBP (11.1 cm water-equivalent depth from the isocenter). This distance between detector and entrance window was checked before each beam time, a time-dependent distance change over the course of one beam time due to a bowing of the entrance window was found to be negligible.

Two different detectors were used over the course of the calorimetric measurements: Detector 1 was used for the first two measurement campaigns in September and November 2019, detector 2 was used for the campaigns in July 2020 and March 2021. Thereby, a possible influence of the detector itself on the measurement result should be excluded, thus, obtaining a more reliable result. The detectors' properties such as distance of the thermistors to the beam axis, thermistors' diameter and resistance are listed in Table 3.

Detector	Thermistor	Resistance / kΩ	Diameter / mm	Horizontal position / mm	B value / K
1	E15	12.0	0.69	+3.44	3248.47
	E18	8.6	0.56	-3.50	3235.08
2	E9	16.3	0.69	-2.19	3233.79
	E12	14.2	0.61	+3.53	3228.34

Table 3: Properties of the water calorimetric detectors that were used for the determination of $D_{w,Q}$. Resistance and material specific value B are valid at a water temperature of 4°C; the given diameter is the one of the glass pipettes tips in which the thermistor was fused.

A thermistor consists of a semiconductor material exhibiting a temperature-dependent resistance change $R_{th}(T)$ according to

$$R_{th}(T) = R_{th,0} \cdot e^{B(1/T - 1/T_0)} \tag{35}$$

with the measured absolute temperature T, the resistance $R_{th,0}$ at a temperature T_0 and a material parameter B. The thermistor's sensitivity S describing the relative resistance change with temperature is given by

$$S = \frac{1}{R_{th}} \frac{\partial R_{th}}{\partial T} = -\frac{B}{T^2}. \tag{36}$$

Each thermistor was calibrated before at PTB, allowing a determination of S with a relative standard uncertainty of 0.07 % [31]. Therefore, during each measurement campaign, the water temperature T was measured using a calibrated PT-100 sensor and recorded throughout the entire measurement. Measuring the relative resistance change $\Delta R_{th}/R_{th}$, the radiation-induced rise in temperature ΔT was determined via

$$\Delta T = \frac{1}{T} \cdot \frac{\Delta R_{th}}{R_{th}}. \tag{37}$$

Each thermistor's resistance was measured individually with a resolution better than 1 mΩ [18] using two independent 1.5 V DC-powered voltage divider circuits with a well-known fixed pre-resistor of about 20 kΩ as one part and the thermistor as the other part. The voltage drop over each part of circuit was measured by high-stability multimeters (Agilent 3588A) within a time interval of 0.1 s. The circuit is shown in Figure 14.

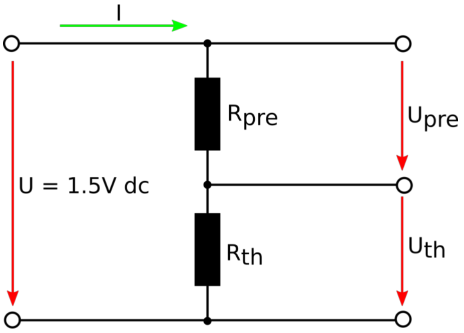

Figure 14: 1.5 V DC-powered voltage divider circuit for the determination of R_{th}.

Since $I = I_{pre} = I_{th}$ for the circuit, it follows for the thermistor's resistance R_{th}

$$R_{th} = \frac{U_{th}}{I} = R_{pre} \cdot \frac{U_{th}}{U_{pre}}, \tag{38}$$

with I_{pre} and U_{pre} denoting the current and voltage in the pre-resistor part of the circuit and I_{th} and U_{th} in the thermistor's part. R_{th} was recorded with 1 Hz as the average over 10 values each.

The calorimetric signal measured during the irradiation is shown in Figure 15. Here, an irradiation causing a rise in temperature corresponds to a decrease in the signal. The signal during a single irradiation of the standard irradiation plan is shown by the embedded picture; it clearly reflects the rescanning of the field as described in Chapter 3.1.4.

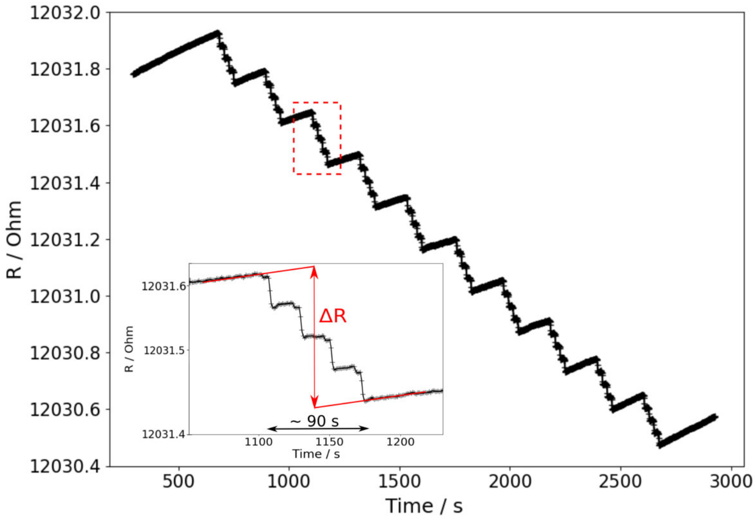

Figure 15: Course of the measurement signal (thermistor probe's resistance R) during a water the calorimetric measurement. The lower left pictures shows a zoom of the signal during one irradiation of the plan (dashed red box) and the determination method of the resistance change ΔR. Reprinted from [3].

The resistance change for each irradiation ΔR was determined at the middle of the irradiation by fitting two linear functions to the signal's course before and after the irradiation. Each fit covers a time window of 110 s starting 10 s after the last irradiated spill. [18]. The standard irradiation plan was irradiated ten times in a sequence with a break of two minutes between each irradiation. This block of irradiation was followed by a mixing of the water of five minutes with a remote-controlled mixer inside the calorimeter and a waiting for about one hour for the temperature distribution to stabilize.

3.4.2 Correction factors for calorimetric measurements

Correction factors were applied for the determination of $D_{w,Q}$ to correct for the following effects:

- **Heat conduction effects** k_c: Heat conduction effects were modeled performing finite-element calculations using the software COMSOL Multiphysics (version 5.4). The heat transport simulation was split into three separate calculations: Within a first calculation, the influence of the actual dose distribution during the experiments was simulated based on the data from the field characterization measurements (see Chapter 4.3.2). The water calorimetric detector's glass cylinder was implemented in the software within a second calculation, but excluding the glass pipettes and the thermistor probes. These were included in a third calculation. This separation was done, as the thin structures of the glass cylinder and additionally of the pipettes within one calculation would require an extremely high spatial resolution leading to very long computation times and memory needed. For the last two calculations, again the dose distribution resulting from the field characterization measurements was simulated. Thereby, the effect of the dose distribution, the glass cylinder and the glass pipettes on the heat conduction could be separated from each other. The resulting k_c was given as the product of the correction factors obtained from these three influencing quantities.
  For the implemented glass tips with the thermistor probes, the mean diameter of 0.64 mm (calculated from the values given in Table 3) was used. As the dependence of the heat conduction on the diameter was known from other calculations performed for the geometry of the PTB water calorimeter [31], an uncertainty contribution could be estimated to account for the deviation of the thermistor probes' diameter from this mean value.
  To further decrease the computation time needed, simplifications concerning the temporal structure of the irradiation were made. The irradiation was devided only in single spills assuming that each part of the field per spill is irradiated at once instead of simulating each single beam spot as a Gaussian distribution. Therefore, an averaged spill / spill break sequence with 2.6 -4.6 s per spill and 4.1 s break was used; these were determined on the basis of the accelerator's beam records. As an estimation of the uncertainty contribution due to this simplification, the results of this simulations were compared to simulations where the entire irradiation field was applied at once (still taking the time structure of spills and spill breaks into

account).
All heat transport correction factors were calculated as the respective mean value of the corrections for the 10 consecutive measurements of one block of irradiations.

- **Heat defect** k_h: The heat defect describes the possible difference between the absorbed radiation energy and the energy that appears as heat, caused by the radiolyses of water. Different studies [95, 96] showed that for high-purified, H_2-saturated water a steady state of the radiolyses' products was reached after a small irradiated dose, which means a zero heat defect and $k_h = 1$. This result was validated also for protons via calculations for a passively scattered [97] and a scanned proton beam [46]. Since no LET-dependence of the heat defect has been found, k_h can be assumed to be unity also for carbon ions. For the PTB water calorimeter at a ^{60}Co beam, it was experimentally shown that the assumption of a zero heat defect is reasonable under the described circumstances within a relative standard uncertainty of 0.14% [31]. Here, the calorimetric detector was pre-irradiated with a dose of about 50 Gy before every measurement campaign; $k_h = 1$ was assumed with a relative standard uncertainty of 0.14% for all measurements.

- **Lateral displacement of the thermistor probes** k_l: The off-axis position of the thermistor probes caused a difference in the measured $D_{w,Q}$ compared to the center position (at which the ICs are positioned), as the dose distribution was not perfectly uniform. As a correction for this effect, the ratio of dose values given at the center of the irradiation field and at the thermistor probes' position was calculated based on the field characterization measurements. The discrete measurement points were interpolated as described in Chapter 3.2.2 to determine the dose values at the thermistors' positions. A correction factor k_l was determined for each thermistor and for each measurement campaign.

- **Measurement depth at different water temperatures** k_d: As the density of water changes with temperature (999.97 kg/m^3 at 4°C, 998.60 kg/m^3 at 18°C), the water-equivalent measurement depth differed for the calorimetric measurements at 4°C water temperature and the ionometric measurements that were performed at 18°C. The dose values at the measurement depth at 4°C and at room temperature were determined via a linear interpolation in depth of the central dose values in the SOBP (taken from the field characterization measurements). The correction factor k_d was calculated as the ratio between these two values.

- **Field perturbation effect** k_p: The calorimetric detector caused a perturbation of the irradiation field. To determine this effect, an IC (PTW TM30013) was positioned inside a glass cylinder identical to the one used for the calorimetric detector. The measured IC reading was compared to measurements under the same conditions, but without the glass cylinder. In total, 22 measurements were performed with and 20 without the glass cylinder. As these measurements do not consider the perturbation effect of the glass pipettes, additional MC simulations were performed as described in Chapter 3.3.1. In addition to the settings and geometrical setup described there, the full glass cylinder as a geometry as well as the glass pipettes approximated by solid glass cylinders with a diameter of 0.5 mm were implemented. The simulations were performed both with the material of the region for the calorimetric detector's glass components set to water and to glass. A detector with a thermistor's dimensions was inserted by a USRBIN card, its output for both materials was compared.

- **Influence of the thermistors' electrical power k_e**: The temperature rise of the thermistor probes due to the change in the thermistors' electrical power during the irradiation influenced the measurement. The corresponding correction factor k_e was calculated theoretically based on the the setup of the resistance measuring circuit (Figure 14), the temperature rise dT_{cal} as it was measured during the calorimetric experiment and the thermal coupling between thermistor and water $\left(\frac{dT}{dP}\right)_{th}$, with dP_{th} denoting the change in the thermistor's power due to the change in the thermistor's temperature dT_{th}. The thermal coupling was known from the temperature calibration of the probes, it is typically in the order of 10^{-3} K/μW. k_e is given as

  $$k_e = \frac{dT_{cal} + dT_{th}}{dT_{cal}}, \tag{39}$$

  with

  $$dT_{th} = dP_{th} \cdot \left(\frac{dT}{dP}\right)_{th}. \tag{40}$$

  From the divider circuit it follows

  $$P_{th} = U_{th} \cdot I = \frac{U_{th}^2}{R_{th}} = \frac{R_{th} \cdot U_{total}^2}{(R_{th} + R_{pre})^2}, \tag{41}$$

  with P_{th} denoting the thermistor's power, U_{th} the voltage in the thermistor's part of the circuit and U_{total} the total voltage, R_{th} the thermistor's resistance and R_{pre} the pre-resistance. Performing the derivation of P_{th} with respect to R_{th}, dP_{th} is given by

  $$dP_{th} = \left(\frac{U_{total}^2}{(R_{th} + R_{pre})^2} - \frac{2U_{total}^2 R_{th}}{(R_{th} + R_{pre})^3}\right) \cdot dR_{th}. \tag{42}$$

  Using Equation 39 together with Equation 40 and 42, k_e was calculated.

3.5 Ionometric measurements

IC measurements were performed directly after the calorimetric measurements and under the same irradiation conditions. Therefore, the water was heated to 18°C water temperature. The IC's reference point was positioned at the central beam axis at the same depth as the thermistor probes of the calorimetric detector. IC reading, water temperature and air pressure were recorded with 1 Hz frequency, which allowed a continuous correction of the IC measurement signal for the present air density. 20-30 measurements for each IC

were performed during each measurement campaign.
Based on the measured IC reading M_{corr} which was corrected for the present air density, the IC reading M_Q needed for the determination of k_Q (Equation 21) was determined as

$$M_Q = M_{corr} \cdot k_{pol} \cdot k_s \cdot k_v, \tag{43}$$

with the correction factors for the polarity effect k_{pol}, the ion recombination effect k_s and the volume effect k_v. All three are representing the respective ratios of the corrections for the radiation qualities Q and Q_0. The correction factors are discussed in detail in Chapter 3.5.2.

3.5.1 Ionization chambers

k_Q factors were determined for two different Farmer type ICs, the PTW TM30013 [98] and the IBA FC65G [99]. Their characteristics are given in Table 4.

Quantity	TM30013 (PTW)	FC65G (IBA)
Active medium	air	air
Active volume	$0.60\,\mathrm{cm}^3$ (r: 3.05 mm, l: 23.0 mm)	$0.65\,\mathrm{cm}^3$ (r: 3.10 mm, l: 23.0 mm)
Reference point (dist. from chamber tip)	13 mm	13 mm
Chamber voltage	400 V (± 500 V max.)	300 V (± 500 V max.)
N_{D,w,Q_0}	$5.3687 \cdot 10^7$ Gy/C	$4.8105 \cdot 10^7$ Gy/C

Table 4: Properties of the ionization chambers used for the determination of k_Q factors. Chamber voltage denotes the voltage at which the chambers were operated and in parentheses the maximum voltage allowed. The calibration factors N_{D,w,Q_0} were determined at ^{60}Co with a relative standard uncertainty of 0.25 % using the PTB's primary standard water calorimeter [31]. Data taken from [98] and [99] as well as from the chambers' calibration certificates.

The ICs' calibration factors N_{D,w,Q_0} were determined again at PTB at the end of this project to check their time stability; the changes in the factors found compared to the factors used within this thesis (as listed in Table 4) lie within the factors' uncertainty.

3.5.2 Correction factors for ionometric measurements

According to Equation 43, the following correction factors were applied in order to determine the corrected IC reading M_Q:

- **Polarity effect** k_{pol}: The polarity effect at beam quality Q, was determined via

$$k_{pol,Q} = \frac{|M_{pos}| + |M_{neg}|}{2 \cdot |M_{pos}|}. \tag{44}$$

M_{pos} and M_{neg} are the IC readings at positive and negative operating voltages, both corrected for air density effects. The correction factors k_{pol,Q_0} at beam quality Q_0 were found in the IC's calibration certificates.

- **Saturation effect** k_s: The correction factor $k_{s,Q}$ in the beam quality Q was determined for each IC according to DIN 6801-1 [13]. The IC reading M was repeated measured at 10 different voltages, each at positive and negative polarity. The inverse of M was plotted against the inverse of the corresponding voltage U. A second-order polynomial was fitted to that:

  $$\frac{1}{M} = a_0 + a_1 \cdot \left(\frac{1}{U}\right) + a_2 \cdot \left(\frac{1}{U}\right)^2 , \tag{45}$$

  from which $k_{s,Q}$ was obtained as

  $$k_{s,Q} = 1 + \frac{a_1}{a_0} \cdot \left(\frac{1}{U_G}\right) + \frac{a_2}{a_0} \cdot \left(\frac{1}{U_G}\right)^2 . \tag{46}$$

  Hereby, U_G denotes the IC's operating voltage. The fit was performed by means of a Python routine using the Optimize module from the SciPy package [85]. Based on [100], a value of 1.001 was used for k_{s,Q_0} at beam quality Q_0.

- **Volume effect** k_v: The IC measurement had to be corrected for a volume effect, as $D_{w,Q}$ is a point-like quantity. Actually, the ICs' spatial dose response functions, as they were presented for photon beams in [101] and for electrons in [102], should be used to determined the volume effect. As these functions are not known for carbon-ion beams, simplified assumptions were made to account for the volume effect in the beam quality Q: $k_{v,Q}$ was determined as the ratio of the relative dose at the IC's reference point and the numerical integral across the IC's cross section, based on the field characterization measurements. As the dose distribution within the IC's volume was smooth and without any steep gradients, this procedure provided a satisfying result. The numerical integral was calculated for both only the single measured data points and the interpolated measurement data (see Chapter 3.2.2), the resulting $k_{v,Q}$ were compared. For the beam quality Q_0, the volume effect was negligible due to a flat dose distribution of the reference ^{60}Co field; therefore, no correction factor k_{v,Q_0} had to be applied and $k_{v,Q} = k_v$.

3.6 Uncertainty estimation

The overall uncertainty budget for the resulting k_Q factors as well as for other quantities were determined according to the Guide to the Expression of Uncertainty in Measurement (GUM) [103] using the software GUM workbench [104]. This software allows the input of user-defined model equations with several input quantities and provides interim results, one result quantity and a budget table which are automatically documented as a report.

4 Development and characterization of the irradiation field

In this chapter the development of an irradiation field suitable for the water calorimetric measurements is presented as well as its characterization using different measurement methods such as ICs and film. This detailed field characterization was indispensable for the following calorimetric measurements as it provided information about the applicability of the irradiation techniques used for water calorimetry, as well as it generated the data basis to determine several correction factors and uncertainty contributions for the determination of k_Q factors.
This chapter is based on article [1]. Furthermore, Chapter 4.2 is based on article [2].

4.1 Optimization of the 2DRM

A 6 x 6 x 6 cm^3 dose cube was required for the water calorimetric measurements. Hereby, the lateral field size specified the 2DRM's total area of 10 x 10 cm^2 and the SOBP width defined the pins' height of 57 mm. The pin base area was optimized in terms of field homogeneity, different base areas and their impact on both the resulting lateral dose distribution and depth dose distribution were tested. The 2DRM's sensitivity to tilting was investigated to estimate the effect of possible positioning inaccuracies on the dose distribution. Two identical 2DRMs were produced and compared to investigate the reproducebility of the printing process.

4.1.1 Depth dose distribution

Dose distributions in depth were measured using the Peakfinder for a 278.29 MeV/u ^{12}C beam in water after passing a 2DRM with a 2 x 2 mm^2, 3 x 3 mm^2 and 4 x 4 mm^2 pin base area, they are shown in Figure 16.
A clear formation of a SOBP with a plateau region of flat dose distribution at z = 85...141 mm can be observed for all 2DRMs. For the 2 x 2 mm^2 pin 2DRM, the SOBP shows a peak at the beginning and at the end of the plateau region, which become smaller for 3 x 3 mm^2 pins and disappear for 4 x 4 mm^2 pins. These peaks are artifacts caused by inaccuracies during the 3D printing process: Due to the hardening of the initially liquid printing material during the printing process, a bending of the pins' tips and a filling of the grooves between the pins may occur. This slightly changes the weights for the contribution of the highest and lowest energy of the SOBP superposition. The printed structures become less fine for bigger pin base areas and the relative printing inaccuracies, and consequently also the artifacts, become smaller.

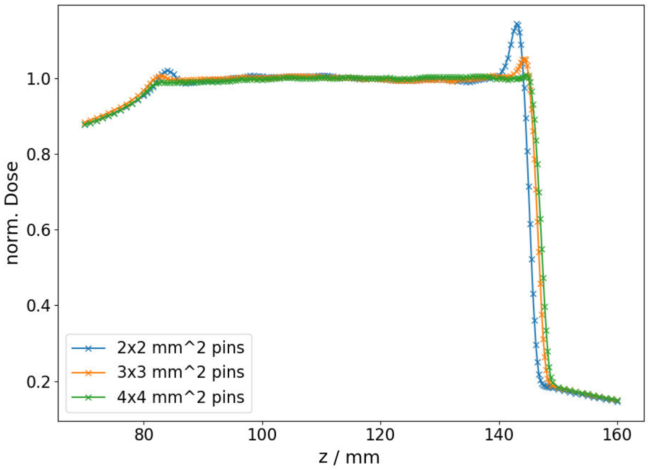

Figure 16: Depth dose distributions for 2DRMs with pin base areas of 2 x 2 mm^2 (blue), 3 x 3 mm^2 (orange) and 4 x 4 mm^2 (green), measured with the PTW Peakfinder. Reprinted from [1].

The relative standard deviations and the relative maximum deviations of the dose values within the plateau region of the SOBP for the three different versions of the 2DRM were calculated, they are given in Table 5. The standard deviation becomes smaller, which means the plateau becomes more homogeneous, the larger the pin base area is.

2DRM	Rel. std. dev. / %	Max. dev. / %
2 x 2 mm^2 pins	0.53	2.08
3 x 3 mm^2 pins	0.44	1.54
4 x 4 mm^2 pins	0.31	1.34

Table 5: Relative standard deviation and maximum relative deviation of dose values measured within the plateau region (z = 85...141 mm) of the SOBP for each 2DRM.

4.1.2 Lateral dose distribution

The pattern of the 2DRM's pins creates a pattern in the resulting dose distribution that becomes increasingly blurred with greater distance from the 2DRM. EBT3 film segments were positioned inside the slab phantom (as described in Chapter 3.2.3) at different depths to investigate this effect. The corresponding positions at the water calorimetric measurement setup are:

- in front of the calorimeter, 65.5 cm in air behind the 2DRM (0.7 mm WET),
- at a 5 cm depth in water inside the calorimeter (60.7 mm WET),

- at a 10 cm depth in water (including the calorimetric detector's glass wall) inside the calorimeter (111.3 mm WET); this position corresponds to the calorimetric measurement depth.

The values given in parentheses are the sums of material's WETs in the beam path between the isocenter (2DRM's backside) and the measurement position. All film segments were corrected using the triple channel analysis, the result can be seen in Figure 17.

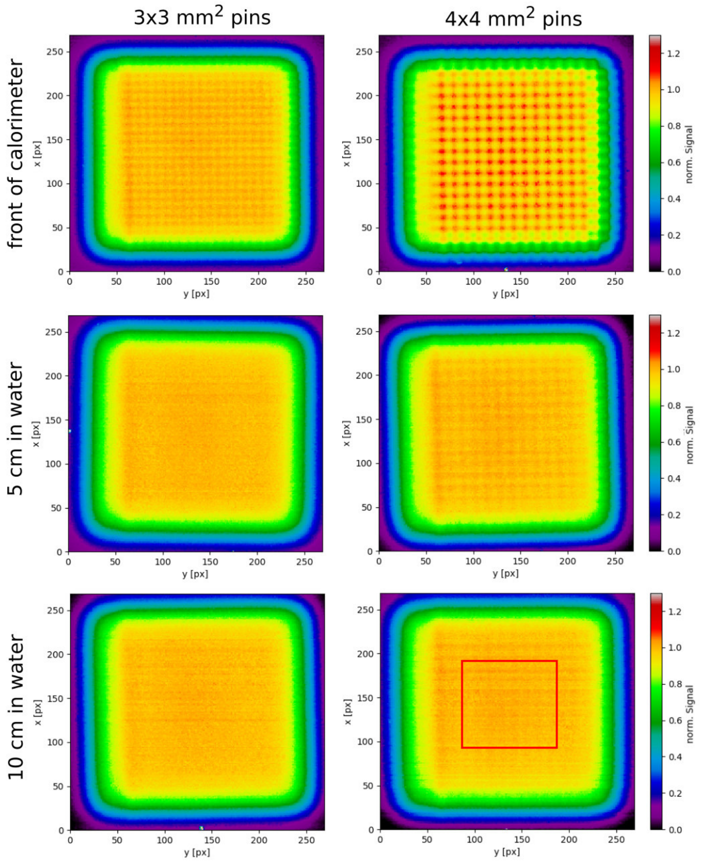

Figure 17: EBT3 film measurements of the lateral dose distributions in front of the calorimeter (top), at a 5 cm depth in water inside the calorimeter (middle) and at a 10 cm depth in water (bottom). Measurements were performed with the 3 x 3 mm^2 (right) and the 4 x 4 mm^2 (left) pin base area 2DRM in the beam path. The inner 100 x 100 px are exemplary indicated by the red square in the lower right picture, standard deviations were calculated for this region. Reprinted from [1].

The pin pattern of both 2DRMs can be clearly seen in the lateral dose distribution in front of the calorimeter. At 5 cm depth, this pattern is completely blurred and invisible for the 3 x 3 mm^2 pin 2DRM. In contrast, for the 4 x 4 mm^2 pin 2DRM, the pattern is still visible at this position and can be even slightly recognized at a 10 cm depth in water. This means that the distance between the 2DRM and the calorimetric measurement position at 10 cm depth in water is not large enough for a homogeneous dose distribution when using the 4 x 4 mm^2 pin 2DRM. For this depth, the relative standard deviations of dose values within the inner 100 x 100 px (= 35 x 35 mm^2) of the film segment were calculated as a measure for the lateral dose distribution's homogeneity. This was 1.32 % for the 3 x 3 mm^2 pin 2DRM and 1.51 % for the 4 x 4 mm^2 pins, indicating a better homogeneity for a small pin base area.

4.1.3 Sensitivity to tilting

The impact of the alignment accuracy of the 2DRM on the dose distribution was investigated. Therefore, each of the three different 2DRMs was set onto the positioning table first accurately aligned to the beam and then tilted by 0.5°, 1.0° and 2.0° around the y-axis. For each position, the depth dose distribution was measured for a 278.29 MeV/u ^{12}C beam using the Peakfinder, the result is shown in Figure 18.

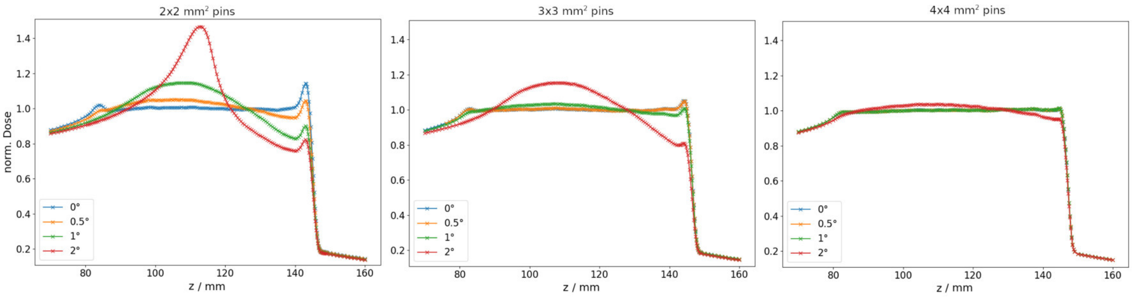

Figure 18: Depth dose distributions for the 2DRMs with 2 x 2 mm^2 (left), 3 x 3 mm^2 (middle) and 4 x 4 mm^2 (right) pin base area. The 2DRMs are aligned (blue) to the beam and tilted by 0.5° (orange), 1.0° (green) and 2.0° (red) around the y-axes. Measurements were performed with the Peakfinder, the data was normalized to the plateau's (z = 85...141 mm) mean value for the aligned 2DRM. Reprinted from [1].

An influence of a misalignment of the 2DRM can be clearly observed: the measured distribution differs more from the aligned 2DRM's distribution the larger the tilting angle is. This effect becomes smaller for a bigger pin base area. For the 2DRM with 2 x 2 mm^2 pin base area, even a titling angle of 0.5° clearly changes the distribution. In contrast, for the 4 x 4 mm^2 pin 2DRM, nearly no difference in the distributions can be observed up to a tilting angle of 1°; the maximum deviation of the distributions in the plateau region for aligned and tilted around 1° 2DRM is 0.5 %.

The lateral dose distribution at the water calorimetric measurement position (10 cm depth in water) was measurement with respect to the tilting angle, using the Octavius inside the water phantom. The one-dimensional distribution across the the x- (y = 0, top) and y-axes (x = 0, bottom) for each of the three 2DRMs can be seen in Figure 19.

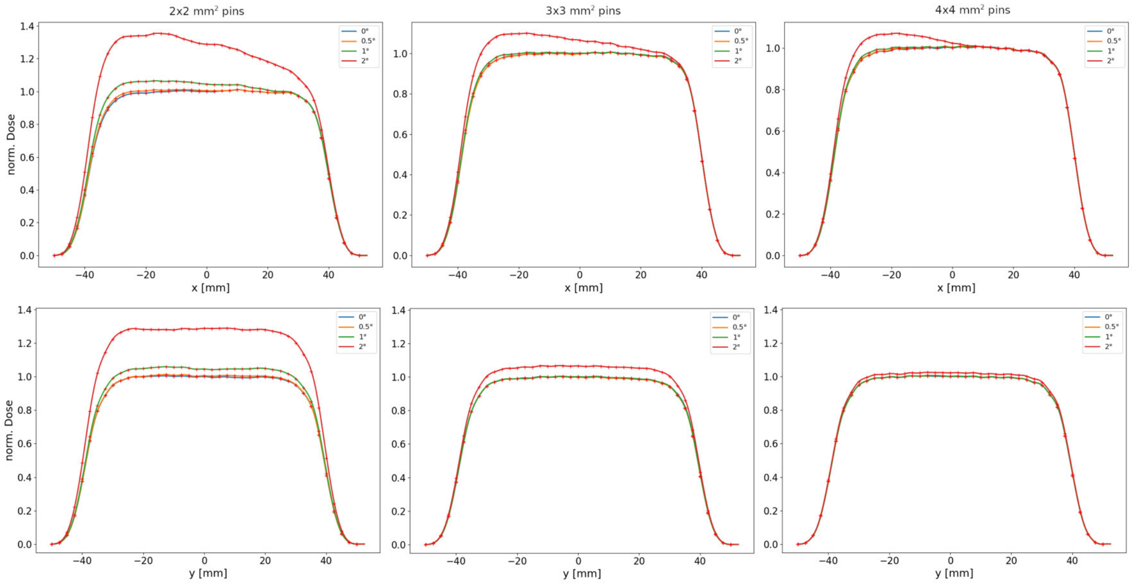

Figure 19: Lateral dose distributions for the 2DRMs with 2 x 2 mm^2 (left), 3 x 3 mm^2 (middle) and 4 x 4 mm^2 (right) pin base area, aligned (blue) to the beam and tilted by 0.5° (orange), 1.0° (green) and 2.0° (red) around the y-axes. Plotted across the x- (y = 0, top) and y-axes (x = 0, bottom). Measurements were performed with the Octavius inside the water phantom at 10 cm depth, the data was normalized to the plateau's (x = -20...20 mm) mean value for the aligned 2DRM.

An increase in the dose towards negative values across the x-axes can be observed. Across the y-axis, the dose distribution stays constant, but the absolute dose rises for large tilting angles. These effects also become smaller for a bigger pin base area. In addition to the experiment, simulations were performed [105] showing that a tilting of the 2DRM does not lead to an oblique lateral profile. Instead, the effect can be explained by a slight misalignment of the Octavius during the measurements. In regions with high gradients as given for the depth dose distributions of the tilted 2DRMs (Figure 18), a misalignment would be clearly visible in the lateral profile. In contrast, for the perfectly aligned 2DRM with a flat depth dose distribution, such a misalignment would not change the lateral distribution visibly.

4.1.4 Comparison of identical 2DRMs

As a good compromise between axial and lateral field homogeneity, the 2DRM with a 3 x 3 mm^2 pin base area was selected for all upcoming measurements. A second, identical

2DRM was produced as a backup and to investigate the reproducibility of the manufacturing process. This 2DRM will be denoted as “version 2”, “version 1” is the $3\,\mathrm{x}\,3\,\mathrm{mm}^2$ pin 2DRM which was used for the measurements described above. Lateral and depth dose distributions were measured also for version 2 of the 2DRM. A comparison of the resulting distributions from both 2DRM versions are shown in Figure 20.

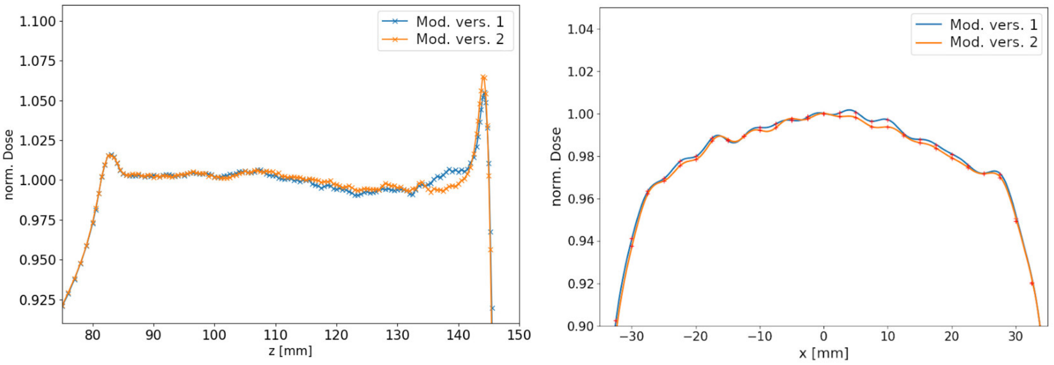

Figure 20: Depth dose distribution (left) and lateral dose distribution (right) for $3\,\mathrm{x}\,3\,\mathrm{mm}^2$ pin 2DRM version 1 (blue) and version 2 (orange). Measurements were performed with the Peakfinder and the Octavius inside the water phantom at 10 cm depth, the data was normalized to each plateau’s mean value.

The two 2DRM versions produce very similar dose distributions both in depth and laterally, although there are small differences. Based on the measurements, the relative standard deviations in terms of depth within the plateau region ($z = 85$ mm and 141 mm) and laterally within a radius around the center of the dose distribution was calculated. Therefore, a radius of 20 mm was choosen, as it is also used as a criteria for field homogeneity (see Chapter 3.1, 4.3.2). In addition, the standard deviation was also calculated for a radius of 15 mm to clarify the difference between both 2DRM versions. The results are given in Table 6.

Rel. standard deviation / %	Modulator version 1	Modulator version 2
in terms of depth	0.44	0.42
laterally (15 mm radius)	1.13	1.00
laterally (20 mm radius)	1.35	1.34

Table 6: Relative standard deviation of measured dose values for the two versions of the 2DRM with a $3\,\mathrm{x}\,3\,\mathrm{mm}^2$ pin base area. Calculated in terms of depth for values within the plateau region of the SOBP (taken from the Peakfinder measurements) and laterally for values within a certain radius around the center of the 2D dose distribution in the middle of the SOBP (measured with the Octavius).

The standard deviations stated are of the same order, both 2DRMs can be used for calorimetric measurements, although slight differences appear. For better comparison, the differences between each measurement point of the normalized distributions created with the two versions of the 2DRM were calculated. These are below 1.1 % within the plateau region for the depth dose distribution and at about 0.4 % for the lateral dose distribution. From that, it can be concluded that the dose distributions created by the two version of the 2DRM must be characterized individually when using both 2DRMs for water calorimetric measurements.

If not stated otherwise, all following measurements were performed with the 3 x 3 mm^2 pin 2DRM version 1. Version 2 was kept as a backup.

4.2 EBT3 measurements

EBT3 film was used for measurements of the lateral dose distribution with a high spatial resolution, as it was needed to investigate the blurring of the 2DRM's pin pattern presented in Chapter 4.1.2. In addition, it was checked if the Octavius' spatial resolution is sufficient for the detailed field characterization, needed for the determination of k_Q. First, a calibration curve was determined to be able to calculate a dose-related quantity from the film's optical density. The triple channel analysis was applied to improve the image quality removing the non-dose related artifacts from the film signal. The resulting film dose distribution was compared with Octavius measurements performed simultaneously with the film stack onto the Octavius.

4.2.1 Calibration of EBT3 signal

Carbon-ion fields of different number of primary particles corresponding to absorbed doses to water between 0.1 and 3.2 Gy were irradiated to one film specimen. The mean optical density value of each fields' central ROI of 56 x 56 px (separated into the three color components red, green and blue) was calculated and plotted against the applied dose, the calibration function (Equation 29) was fitted to that. The same was done to calibration fields irradiated with photons using a LINAC for comparison. The resulting calibration curves for each color channel are shown in Figure 21. The corresponding fitting parameters and the normalized root-mean-square errors (RMSEs) of the fit are given in Table 7.

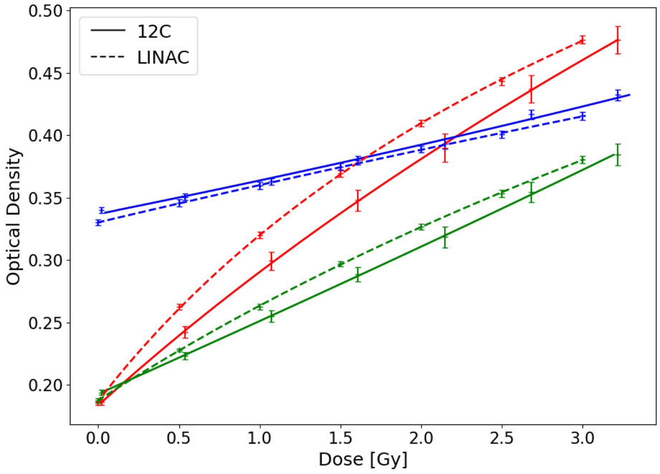

Figure 21: Calibration curves for the red, green and blue color channel of EBT3 film specimens irradiated with carbon ions (solid lines) and photons (dashed lines). Error bars show the standard deviation of the pixel values from each other within the central ROI. Reprinted from [2].

Channel	a	b	c	RMSE / %
Red	2.14 ± 0.03	0.00106 ± 0.00006	3.19 ± 0.05	0.92
Green	6.10 ± 0.15	-0.028 ± 0.018	9.40 ± 0.23	0.76
Blue	9.3 ± 0.3	-0.196 ± 0.018	20.0 ± 0.6	3.49

Table 7: Fitting parameters for equation (29) with one standard deviation errors and normalized RMSEs for ^{12}C-irradiated film.

The calibration curves fit the data points very well. Comparing the calibration curves based on the carbon-irradiated film (Figure 21, solid lines) with the curves based on photon-irradiated film (Figure 21, dashed lines), they show a similar course: The red curves have the steepest gradient and cross first the green and then the blue curves. However, the calibration curves of the photon-irradiated film are above the curves for ^{12}C-irradiated specimens for the red and green color channel, corresponding to a higher signal of the photon-irradiated film specimens to the same applied dose. A decreased response of EBT to carbon ions compared to photons was also observed by Martisikova *et al.* [73], they found a response to carbon ions at about 70 % of the response to photons. Here, the optical density of the carbon-ion irradiated film was at 90 - 96 % of the photon-irradiated OD for the red color channel and at minimum 94,% for the green color channel. In contrast, for the blue color channel, a higher response of the carbon-ion-irradiated film compared to the photon-irradiated film was observed. The calibration curves of LINAC-irradiated and ^{12}C-irradiated film show a slightly different slope, especially for the red color channel. Due to these differences, it can be concluded that calibration parameters for EBT3 measurements with carbon-ion beams should always be taken from ^{12}C-irradiated film specimens.

Uncertainty budget A standard uncertainty for the film measurements was determined based on the uncertainty of the calibration and the correlation of the fitting parameters determined from the fit's covariance matrix. The mean relative standard deviation of 3.2 % of repeated film measurements at the same measurement position was taken into account as the uncertainty of the film signal. The uncertainty budget was calculated according to the GUM [103] using GUM workbench [104], it is given in Table 8. As the resulting dose values are determined from the red color channel, the budget was calculated only for this channel.

Quantity	Rel. standard uncertainty / %
Film signal OD	3.2
Calibration	
Fitting parameter a	1.6
Fitting parameter b	5.5
Fitting parameter c	1.7
Dose D	**8.9**

Table 8: Combined standard measurement uncertainty budget for the absorbed dose to water determined from the red color channel of EBT3 film measurements.

4.2.2 Correction using the triple channel analysis

Dose distributions measured with EBT3 film were corrected applying the triple channel analysis as described in Chapter 3.2.1. A comparison of the original, uncorrected dose distribution and the corrected one are shown in the figures 22 and 23. The film specimens were irradiated with the standard plan described in Chapter 3.1.4 using the 2DRM.

The one-dimensional corrected dose distribution shows a quite constant course within the plateau region of the field, whereas the uncorrected distribution drops at higher x-values. A very sharp peak can be seen in the uncorrected distribution at x = 122, which vanishes in the corrected signal.

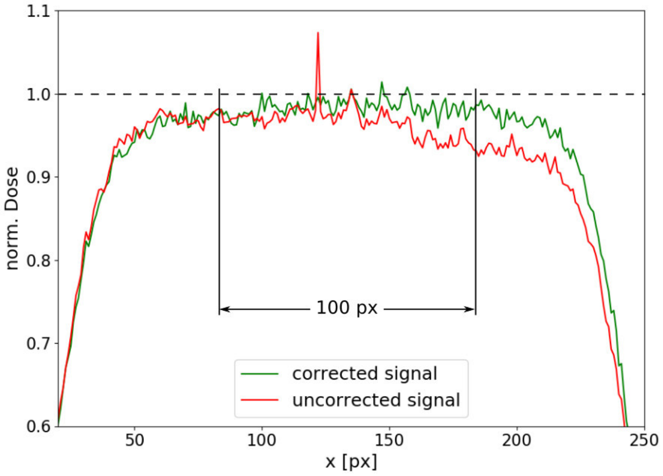

Figure 22: Comparison of an uncorrected (red) and corrected (green) film dose distribution, plotted in one dimension, taken from the center of the film specimens positioned at the middle of the SOBP. Dose values were normalized to the central dose value of each signal. Coordinates are given as pixel numbers. Reprinted from [2].

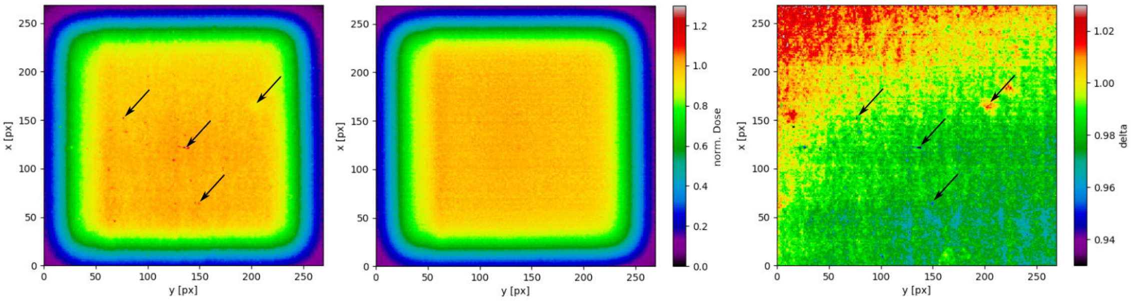

Figure 23: 2D dose distributions of an uncorrected (left) and corrected film signal (middle) as well as the distribution of the corresponding disturbance value δ (right). Arrows show artifacts in the uncorrected film as well as their reflection in the distribution of δ. Dose distributions were normalized to the maximum; coordinates are given as pixel numbers. The film specimens were positioned at the middle of the SOBP. Reprinted from [2].

Several artifacts (marked by the arrows) can be observed in the uncorrected dose distribution, the signal drops slightly to the upper left. In contrast, the corrected distribution shows a rather homogeneous signal without artifacts. Both the artifacts and the signal drop are clearly reflected in the distribution of the disturbance value δ. The standard deviation (maximum deviation) for the inner 100 x 100 px (= 35 x 35 mm^2) is 1.9 % (28.6 %)

for the uncorrected signal and 1.3 % (9.8 %) for the corrected signal.
A higher signal can be observed on the left side (y ≈ 60 px) for both the corrected (Figure 23, left) and the uncorrected distribution (Figure 23, middle), it is not reflected in the δ distribution (Figure 23, right). This increased signal was caused by additional material in the beam path (0.5 mm PMMA, backside of the 2 cm tall 2DRM holder, was removed later). The ratio between the signal in this area and the signal in the middle of the field (between x, y = 85...185 px) is 1.038 for the uncorrected distribution and at 1.033 for the corrected distribution.
Applying the triple channel analysis, artifacts are removed from the film dose distribution, as it is also reflected in the lower maximum deviation of the inner measurement points for the corrected signal compared to the uncorrected. The artifacts were caused by contaminations in the film specimens such as impurities within the film or dust particles on the film or the scanner. The asymmetric distribution dropping from low to high x-values in Figure 22 and from the upper left to the lower right in Figure 23 (left) can be explained by a variation in the film thickness or an asymmetry in the scanning system. This is also compensated by the triple channel analysis, the drop is not observable in the corrected film signal. However, the increased signal at y ≈ 60 px (Figure 23, left and middle), which is not related to any film or scanning artifacts, but is an actual inhomogeneity in the applied dose distribution itself, is not affected by the correction.

4.2.3 Comparison between EBT3 and IC array signal

EBT3 film specimens were stuck onto the Octavius to measure the dose distribution simultaneously with both devices. As the Octavius ICs' effective measuring point is at 5.5 mm water-equivalent depth beneath the array's surface, the measurement depth of the film specimens differs slightly from the Octavius'. However, as the depth dose distribution shows a very flat course in the middle of the SOBP (see Chapter 4.1.1), this slight difference in the measurement depths can be neglected. The Octavius was positioned behind the slab phantom at the calorimeter's measurement position to measure at the middle of the SOBP, and irradiated with the standard irradiation plan using the 2DRM. The film signal was averaged over the inner seven rows of pixels which correspond to a width of 2.5 mm, to match the IC dimensions of the Octavius. Four repeated measurements were performed and averaged, their relative standard deviation was 3.2 % for the film and 0.2 % for the Octavius. The resulting 1D dose distributions across the x-axes are shown in Figure 24. Each data set was normalized to its central value; the pixel numbers were converted to mm to fit them to the coordinates of the Octavius data. The Octavius was calibrated for the relative response of its individual chambers beforehand as presented in Chapter 4.3.1.

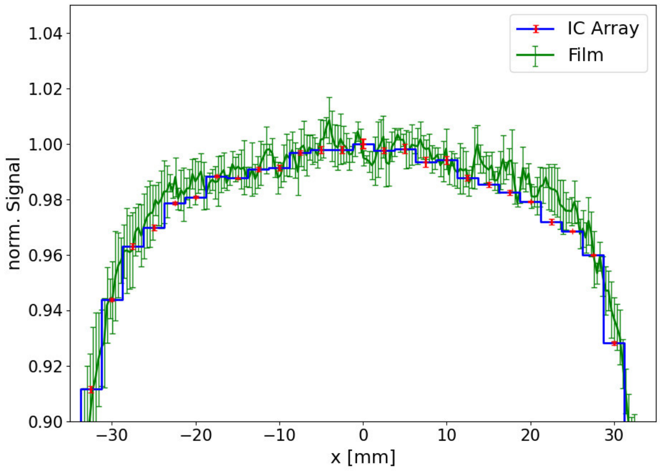

Figure 24: Comparison of dose distributions measured simultaneously with EBT3 film and the Octavius. Error bars give the standard deviation of the repeated measurements from which the average was plotted. Reprinted from [2].

The distributions agree very well, differences are within the standard deviation of the repeated film measurements. The standard deviation and the maximum deviation of the measured data points in the inner $35 \times 35\,\mathrm{mm}^2$ (corresponding to 100×100 px) was calculated for both distribution. For the Octavius data, this is 0.8 % with a maximum deviation of 3.1 %; for the film data a standard deviation of 1.3 % and a maximum deviation of 9.8 % was found. The higher standard deviation in the film signal compared to the Octavius can be explained by a volume averaging in the Octavius' ICs leading to a smaller contribution of high spatial frequencies. This is also reflected by the noisier film signal compared to the Octavius signal.

A gamma index analysis with a 3 mm (3 %) criterion was performed for a quantitative comparison of Octavius and film data. It gave a pass rate of 85.4 % when all measurement points are considered and 97.6 % when only taking points with dose values $> 10\,\%$ of the maximum dose into account. As only the high-dose plateau region is of interested for the field characterization measurements, the gamma pass rate is satisfying. These results show, that the Octavius provides a sufficient spatial resolution to be used for field characterization measurements.

4.3 Field characterization

The experimental k_Q factors determined by calorimetric and ionometric measurements are influenced by the dose distribution around the measurement position. Therefore, a detailed characterization of the three-dimensional dose distribution had to be performed including repeated measurements as a measure for the distribution's time stability. Based on this measurements, correction factors for the calorimetric (Chapter 5.1.1) and ionometric measurements (Chapter 5.2.1) as well as uncertainty contributions to the overall standard uncertainty of k_Q (Chapter 5.3.2) were determined.

4.3.1 Calibration of the IC array's relative response

The Octavius was calibrated for the relative response of its chambers. Therefore, it was irradiated at a well characterized 6 MV photon field at PTB Braunschweig as described in Chapter 3.2.2. Different doses between 0.5 and 5.0 Gy were applied. As no systematic dependency of the Octavius' relative response on the dose within this dose range could be observed, the Octavius data was averaged over all measurements. The comparison with the PTB data of the irradiation field can be seen in Figure 25.

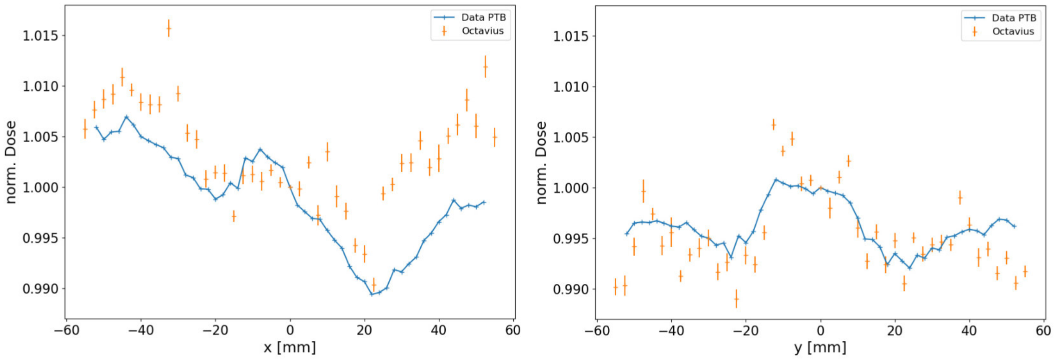

Figure 25: Comparison between the PTB measurement data (blue) and the Octavius signal (orange) at the PTB 6 MV photon field. The data was normalized to the central value (x, y = 0) and plotted in one dimension across the x- (y = 0, left) and y-axes (x = 0, right). Error bars indicate the standard deviation of repeated measurements.

A correction factor for each IC of the Octavius was determined as the ratio between the PTB measured dose value at the IC's position and the Octavius IC's measured value. All correction factors were saved to a calibration file, which was then applied to all data measured with the Octavius within this thesis. A standard uncertainty of this correction factors of 0.34 % was estimated based on the standard deviation of the repeated PTB and Octavius measurements.

4.3.2 Repeated IC array measurements

To measure the 3D dose distribution, the Octavius was positioned inside the water phantom setup as described in Chapter 3.2.2. To fully cover the SOBP, the Octavius' depth in water was adjusted in steps of 2.5 mm over a width of 80 mm. For each version of the 3 x 3 mm^2 pin 2DRM, seven measurements were performed over a period of time of 10 weeks as a data basis to evaluate the irradiation field's homogeneity and reproducebility. During the calorimetric measurement campaigns, additional field characterization were performed to assure a certain time stability.

A measured dose distribution for the 2DRM version 1 can be seen in Figure 26. Each data set was normalized as described in Chapter 3.2.2. Depth dose distributions were determined from the 3D dose distributions as described in Chapter 3.2.2 to compare them with the Peakfinder data. Both data sets agree very well, which indicates a good positioning stability of the Octavius when moved in depth.

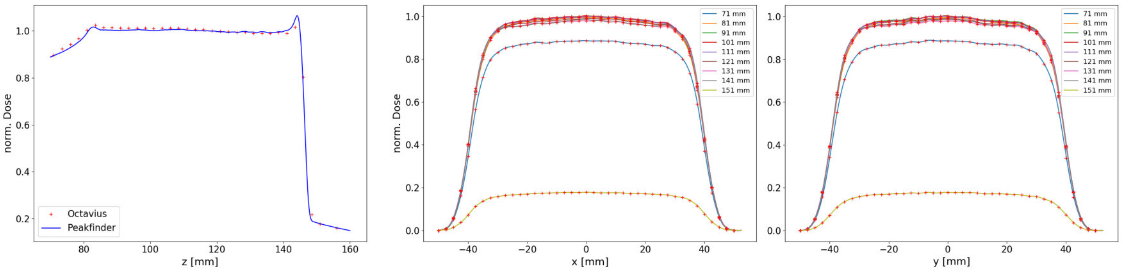

Figure 26: Dose distributions for 2DRM version 1 measured using the Octavius water phantom setup for the characterization of the irradiation field. Left: Comparison of the depth dose distribution measured with the Octavius and the Peakfinder, coordinates given as WEPL from the isocenter. Middle/right: Lateral dose distributions for different depths across the x-/y-axes, normalized to the mean dose within a 20 mm sphere around the center of the dose distribution (x = 0 mm, y = 0 mm, z = 60 mm). Reprinted from [1].

Measurement	Modulator vers.	Rel. std. dev. / %
05-19-19	1	0.78
05-21-19	1	0.97
05-21-19	1	0.83
05-23-19	1	1.03
05-31-19	1	1.05
06-25-19	1	0.78
07-31-19	1	0.91
05-19-19	2	0.71
05-21-19	2	0.92
05-23-19	2	1.00
05-23-19	2	0.98
05-31-19	2	1.02
06-25-19	2	0.86
07-31-19	2	0.85

Table 9: Relative standard deviation of dose values measured within a sphere with a 20 mm radius around the calorimetric measurement position for each field characterization measurement.

The standard deviation of the dose values measured within a sphere with a 20 mm radius around the center of the 3D dose distribution (5164 data points) was calculated as a value for the field's homogeneity. The values for each measurement, given in Table 9, are all below 1.1 %. This indicates a flat and homogeneous irradiation field around the calorimetric measurement position.

For every single measurement point within the 20 mm sphere, the standard deviation between the repeated measurements was calculated. The average of this standard deviation was used as a criterion for the reproducebility of the relative dose distribution. This is 0.26 % for both versions of the 2DRM, which means that the field is quite stable over the given period of time.

4.4 Time stability of the delivered absolute dose

The evolution of the dose delivered by the accelerator was investigated performing IC measurements at the isocenter for the mono-energetic standard irradiation plan (e.g. without 2DRM), as described in Chapter 3.2.4. The IC reading corrected for air density for each measurement is shown in Figure 27.

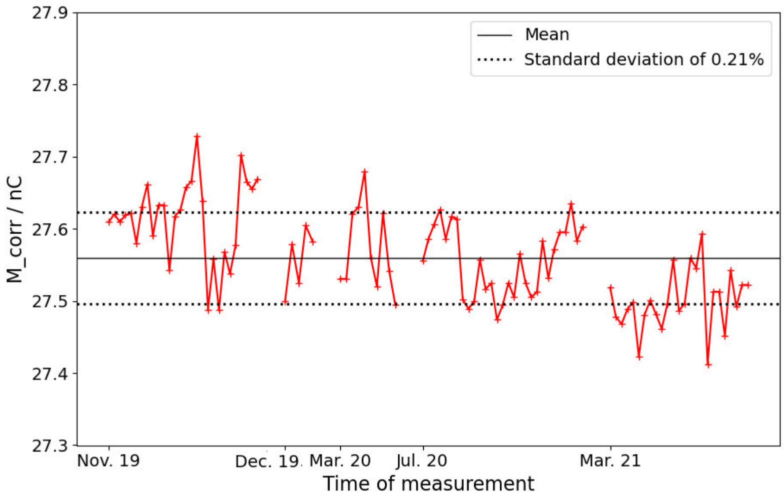

Figure 27: Plot of the IC reading corrected for air density, measured over a period of time of 16 months for the investigation of the delivered dose's time stability. The IC was positioned at the isocenter inside a slab phantom and irradiated without 2DRM in the beam path. The solid line indicates the mean value, dotted lines indicate the standard uncertainty of the measured values.

A relative standard deviation of 0.21 % of the measured values was determined, which was later used as an uncertainty contribution due to fluctuations in the dose application to the uncertainty budget of k_Q (Chapter 5.3.2).

4.5 Monte Carlo simulations

Monte Carlo simulations were performed using the FLUKA code to analyze the particle spectrum at the measurement position and compare it to the one of an actively scanned SOBP. This should give a rationale to transfer the k_Q factors determined for the passively 2DRM-modulated SOBP to an actively scanned one, as it is prevalent in clinics. For all simulations, a pin base area of 3 x 3 mm^2 was used for the 2DRM implemented as it was also used for the calorimetric measurements. 200 000 particles were simulated each for all results shown.

As the 2DRM was implemented as a pixel geometry, first, different pins' voxel resolutions were tested. To investigate how good the implemented setup reflects the experimental situation, depth dose distributions in water were recorded and compared to Peakfinder measured distributions. Therefore, a simplified geometry was used only consisting of the ripple filter, the implemented 2DRM and a water tank, in which the dose was radially scored over an area with 4.08 cm radius and 50 cm length in depth, corresponding with the Peakfinder measurement. The result is shown in Figure 28.

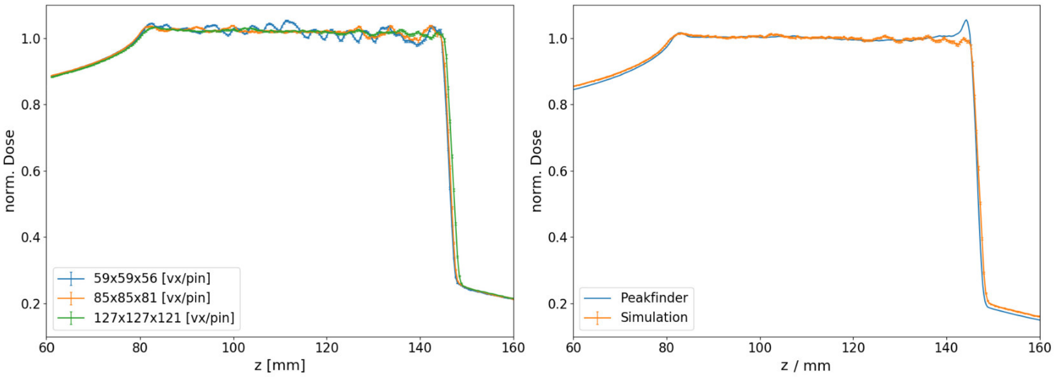

Figure 28: Left: FLUKA simulated depth dose distributions a of 278 MeV/u ^{12}C-beam in water for 2DRM resolutions of 59 x 59 x 56 vx/pin (blue), 85 x 85 x 81 vx/pin (orange) and 127 x 127 x 121 vx/pin (green). Right: Depth dose distribution resulting from the 127 x 127 x 121 vx/pin 2DRM compared to Peakfinder measurement data. All data sets were normalized to the SOBPs (z = 85...141 mm) mean value, z is given as geometrical depth as defined in the FLUKA geometry (Figure 9).

The simulated depth dose distribution is very noisy within the plateau region for the smallest resolution (59 x 59 x 56 vx/pin), getting flatter with with increasing resolution. Compared to the Peakfinder data, the simulated distribution (for 127 x 127 x 121 vx/pin) is slightly noisier towards the end of the SOBP. The peak at the end of the SOBP observed in the experiment is not reflected in the simulation, as the 2DRM's inaccuracies are not implemented here. Nevertheless, both data sets agree very well especially in the middle of the SOBP, which is the region of interest for the calorimetric measurements.

Due to a limitation of the voxel geometry within the FLUKA code, the 2DRM's resolution was limited to a maximum resolution of 160 x 160 x 152 vx/pin. This raises the question of how reliable the particle spectra resulting from a simulation with such a limited resolution are. To investigate this, the resolution's impact on the particle spectra was tested. Particle spectra at the middle of the SOBP in water (simplified geometry as described above) were recorded for resolutions between 59 x 59 x 56 vx/pin and 160 x 160 x 152 vx/pin. Comparing the results for pins with a resolution of 59 x 59 x 56 vx/pin to pins with a 127 x 127 x 121 vx/pin resolution, all differences in the dose, fluence and LET spectra are below 1.5 % for $Z \leq 6$. Even smaller deviations of below 1 % can be observed, when comparing the 127 x 127 x 121 vx/pin resolution to the highest resolution available (160 x 160 x 152 vx/pin). From this result, it can be concluded that even a resolution higher than 160 x 160 x 152 vx/pin would not change the result significantly, justifying the use of a voxelized 2DRM.
Simulations were performed including the entire calorimeter geometry as shown in Figure 9 to obtain particle spectra under the calorimetric measurement conditions. Therefore, a pin resolution of 127 x 127 x 121 vx/pin was choosen, as it could be shown that the resulting spectra only slightly changes when using the highest resolution possible instead, but the computational time dramatically increases. The resulting particle spectra in terms of absorbed dose to matter and fluence can be seen in Figure 29.

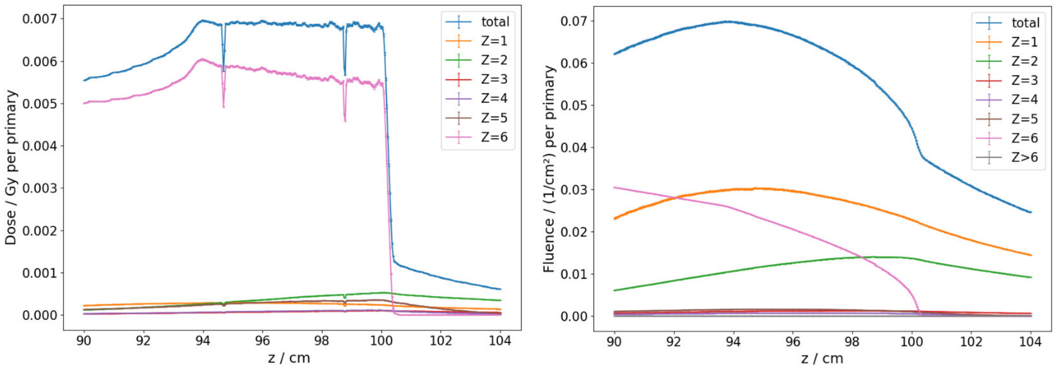

Figure 29: FLUKA simulation result: Distribution of dose (left) and fluence (right) in depth for a 278 MeV/u ^{12}C-beam for the calorimeter setup. z is given as geometrical depth, as it is defined in the FLUKA geometry (Fig. 9). Reprinted from [1].

Two very significant drops within the SOBP can be seen in the dose distribution, they appear at the position of the calorimetric detector's glass walls and can be explained by a difference in the mass stopping power of glass compared to water resulting in a lower absorbed dose. This effect was also taken into account for the heat transport calculations (Chapter 5.1.1).
The percentage in dose and fluence, as well as the LET per particle type around the calorimetric measurement position ($96.7\,\text{mm} \leq z \leq 96.8\,\text{mm}$ in Figure 29) were determined. In addition to the 2DRM SOBP, this was also done for particle spectra simulated for an

actively scanned SOBP as described in Chapter 3.3.1. The results for both SOBPs are given in Table 10.

Z	$N_i/\sum N_i$ / %	D_i/D_{all} / %	$\overline{LET}$ / keV/μm
1	44.77 (47.66)	4.08 (4.49)	0.98 (1.00)
2	20.55 (19.37)	5.77 (5.72)	3.01 (3.12)
3	1.98 (1.83)	1.18 (1.16)	6.41 (6.68)
4	1.10 (1.00)	1.32 (1.22)	12.52 (12.90)
5	2.48 (2.07)	4.57 (3.91)	19.85 (19.96)
6	28.98 (27.97)	82.97 (83.39)	30.81 (31.56)
rest		0.11 (0.13)	

Table 10: Mean percentage of fluence and dose, and track-weighted LET per particle type at the measurement position for the 2DRM-modulated SOBP and in parentheses for the actively scanned SOBP.

For the 2DRM-modulated SOBP, most of the particle within the investigated area around the measurement position are protons, deuterons and tritons with Z = 1, only 30 % of the fluence are carbon ions. However, due to the difference in LET, the dose is mainly deposited by carbon ions (83 %), whereas particles with Z = 1 only provide 4 % to the total dose. Helium ions (Z = 2) make up 20 % of the fluence, contributing 6 % of the dose. The other particles lighter than carbon, Lithium (Z = 3), Beryllium (Z = 4), and Boron (Z = 5), together deposit about 7 % of the dose. Target fragments with $Z > 6$ contribute with only 0.1 % to the total absorbed dose.

Comparing the 2DRM SOBP's particle spectra with the ones resulting for the actively scanned SOBP (Table 10, values in parenthesis), only small differences appear. For the actively scanned SOBP, the percentage of fluence for particles with Z = 1 is 3 % higher (7 % relative increase); for other particles it is between 0.2 % and 1.2 % lower. Particles with Z = 1 and Z = 6 contributed 0.4 % more to the total dose in the actively scanned SOBP which means a relative increase of 10 % (Z = 1) and 0.5 % (Z = 6). The maximum relative difference in LET is about 4 % .

5 Experimental determination of k_Q by means of water calorimetry

In this chapter the experimental determination of k_Q factors based on the development and findings described in Chapter 4 is presented. This includes the calorimetric and ionometric measurements as well as the determination of an overall uncertainty budget for k_Q.
This chapter is based on article [3].

5.1 Calorimetric measurements

Within each measurement campaign, two night shifts of calorimetric measurements were done, performing in total 282 calorimetric measurements within four campaigns. The radiation-induced rise in temperature ΔT was determined from the measured resistance change ΔR as described in Chapter 3.4.1. Figure 30 shows the course of the resulting values of ΔT from both thermistors over all calorimetric measurements.

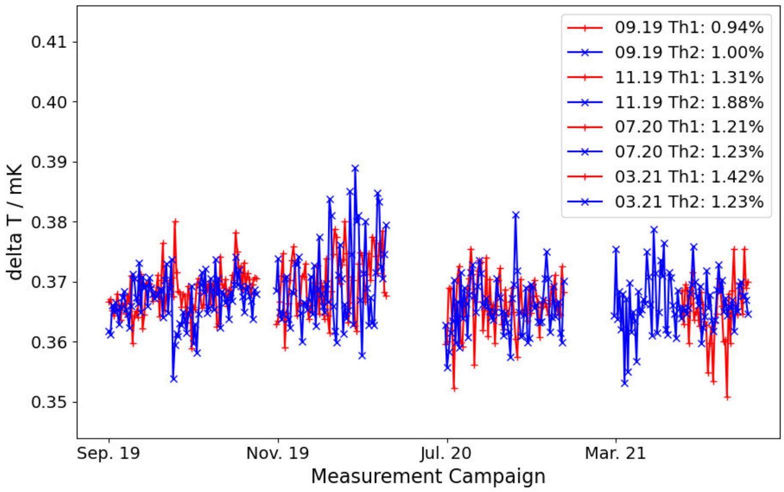

Figure 30: Plot of ΔT determined from the measured thermistors' resistance change ΔR of the calorimetric detector for each irradiation. The legend gives the relative standard deviation of the ΔT values for each measurement campaign and each thermistor. Reprinted from [3].

A statistical distribution of the measured ΔT values appears, no trends can be identified. This indicates that the measurements were not influenced by systematic errors, such as an unstable response of the detector, which could be e.g. cause by an insufficient pre-irradiation of the calorimetric detector resulting in a non-zero heat defect. The use of the mean value of ΔT for each campaign for the determination of $D_{w,Q}$ is justified by this result.

5.1.1 Determination of calorimetric correction factors

Table 11 summarizes the correction factors needed for the calorimetric measurements and their uncertainties, which were determined as described in Chapter 3.4.2.

Correction factor	Value	Rel. standard uncertainty / %
Heat transport effects k_c	0.9979	0.40
Heat defect k_h	1.0	0.14
Lateral displacement k_l		
Sep. 2019 (Detector 1)	1.0005; 1.0021	0.14
Nov. 2019 (Detector 1)	1.0008; 1.0049	0.14
Jul. 2020 (Detector 2)	1.0007; 1.0023	0.14
Mar. 2021 (Detector 2)	1.0026; 1.0027	0.14
Measurement depth at different water temperatures k_d	1.0001	0.10
Perturbation effect k_p	1.0	0.11
Influence of the thermistors' electrical power k_e		
Sep. 2019 (Detector 1)	1.0003; 1.0004	0.01
Nov. 2019 (Detector 1)	1.0003; 1.0004	0.01
Jul. 2020 (Detector 2)	1.0002; 1.0001	0.01
Mar. 2021 (Detector 2)	1.0002; 1.0001	0.01

Table 11: Determined correction factors for the calorimetric determination of $D_{w,Q}$ and their relative standard uncertainties. If two values are given, different values for the two thermistors were found. The factors are valid for both detectors used except for k_l and k_e, where different values were applied for each measurement campaign due to small deviations in the measured dose distributions and different characteristics of the detectors used.

Heat transport effects Heat transport simulations were performed as separate finite-element calculations obtaining the influence of three separate quantities described below. Calculations were performed for different dose distributions to reflect variations in the irradiated field, and varying detector positions caused by positioning uncertainties. The correction factors are calculated as the mean value of the respective results, the measurement uncertainty is given by their standard deviation. The correction factor k_c was determined as the product of the factors resulting from the three quantities:

- The calculation including the real dose distribution of the irradiated field gave a factor of 1.0011 for the heat transport correction. The corresponding standard uncertainty of 0.10 % includes the uncertainty contribution due to fluctuations in the dose distribution as different measured dose distributions were used for the simulations.

- The influence of the detector's glass walls yields in a correction factor of 0.9996 with a standard uncertainty of 0.03 %.

- The glass pipettes enclosing the thermistor probes cause a heat transport correction factor of 0.9972, showing a standard uncertainty of 0.01 %. Here, the mean diameter of the thermistor probes' glass tips of 0.64 mm was used. Based on the maximum deviation of the thermistor probes' diameter from this mean value, an additional uncertainty contribution of 0.08 % to the overall uncertainty of the resulting k_c was estimated.

These factors result in a k_c of 0.9979 with a standard uncertainty of 0.40 %. As the irradiation's time structure was approximated as an irradiation of full spills at once instead of single-point irradiation, an additional uncertainty contribution of 0.15 % was included in k_c's uncertainty, as well as a contribution due to the different parameters used for the calculation of 0.15 %.

Heat defect A zero heat defect ($k_h = 1$) was assumed as the calorimetric detector was filled with hydrogen-saturated water and pre-irradiated with about 50 Gy before each beam time. Following the results for the PTB water calorimeter from Krauss [31], a standard uncertainty of 0.14 % was assumed.

Lateral displacement Due to the their different positions, k_l was determined for every thermistor position individually based on the respective field characterization measurement performed before the measurement campaign. This data was interpolated as described in Chapter 3.2.2; from that, the dose values at the measurement position at the central beam axis and at the position of the thermistor probe were determined; k_l was then determined as the ratio of both values. Its standard uncertainty of 0.14 % is given by the standard deviation of all k_l values determined to take possible fluctuation of the dose distribution into account. A positioning uncertainty of the calorimetric detector and thereby of the thermistor probes was considered in an additional uncertainty contribution to the overall uncertainty budget of k_Q (see Chapter 5.3.2).

Measurement depth at different water temperatures Due to the temperature-dependent density of water, a shift in depth of 0.146 mm has to be taken into account when measuring at 4°C and at room temperature (18°). The corresponding correction factor k_d was determined based on the depth dose distribution taken from the field characterization measurements. Therefore, a linear function was fitted to the plateau region ($90\,\mathrm{mm} \leq \mathrm{z} \leq 140\,\mathrm{mm}$). The resulting gradient of -0.9 mGy/mm gives a difference in dose values of 0.013 % for the shift in depth of 0.146 mm. k_d is given as the ration of dose values at the measurement depth at 4°C and at 18°. A standard uncertainty of 0.10 % was estimated on the basis of the linear fit's uncertainty and the variations between the repeated field characterization measurements used for the fit.

Perturbation effect The field perturbation effect due to the calorimetric detector was experimentally determined measuring with an IC inside the glass cylinder and comparing this to IC measurements without the glass cylinder. The difference between both measurement situations was found to be in the same order as its uncertainty. This result was proofed by the MC simulations performed, which also considered the effect of the detector's glass pipettes. Therefore, k_p was assumed to be one. Its standard deviations is mainly influenced by the standard deviation of repeated measurements, but also the positioning uncertainties of the IC inside the calorimeter was taken into account. An additional uncertainty contribution of 0.1 % was considered due to the approximation of the detector's glass pipettes in the simulation. This leads to an overall uncertainty of 0.11 %.

The very small field perturbation can be explained by a low scattering behaviour of heavy primary particles. As shown in the MC simulations for the particle spectra (Chapter 4.5), heavy particles make up the majority in the beam at the measurement position. This means, only the very thin front walls of the cylinder play a role in the field perturbation, but this is mainly noticeable as a change in the maximum range of the particles.

Influence of the thermistors' electrical power k_e was calculated individually for each thermistor within each measurement campaign, as they all have a different resistance and show a different thermal coupling between thermistor and water, and as the resistance change slightly between the campaigns. The standard uncertainty of 0.01 % is affected by the standard uncertainty of the measured temperature rise, the thermistors' resistance, the resistance change as well as the uncertainty of the thermistors' sensitivity.

5.2 Ionometric measurements

Within each measurement campaign, the two night shifts of calorimetric measurements were directly followed by two night shifts of ionometric measurements, where 20-30 measurements for each chamber were performed at its operating voltage to determine M_Q (see Equation 21). In addition, IC measurements were performed at a negative operating voltage to examine the polarity effect, and at different voltages between 100 V and the maximum voltage allowed for the actual chamber for the investigation of the saturation effect. For all IC measurements, the IC's reference point was positioned at the calorimetric measurement depth at the center of the irradiation field. The water temperature inside the calorimeter was at about 18°C, it was measured throughout the entire measurements, as was the air pressure to be able to correct each IC measurement for the effect of the current air density determining M_{corr}. For the TM30013, M_{corr} showed a mean relative standard deviation of the measured values of 0.16 %; for the FC65G, this was 0.12 %.

Unfortunately, the data measured with the TM30013 within the first measurement campaign could not be used due to a broken connection cable as it was found later. Therefore, this data was excluded form the following results.

5.2.1 Determination of ionometric correction factors

The correction factors determined for the correction of the ionometric measurements as well as their relative standard uncertainties are listed in Table 12.

Correction factor	TM30013	FC65G	Rel. standard uncertainty / %
Polarity effect k_{pol}	1.0015	0.9998	0.08
Saturation effect k_s	1.0028	1.0056	0.20
Volume effect k_v			0.21
Sep. 2019	1.0037	1.0037	0.21
Nov. 2019	1.0067	1.0067	0.21
Jul. 2020	1.0031	1.0031	0.21
Mar. 2021	1.0053	1.0053	0.21

Table 12: Correction factors and corresponding relative standard uncertainties for the ionometric measurements for each IC.

Polarity effect The correction factor for the polarity effect at beam quality Q was determined according to Equation 44 by measuring at positive and negative operating voltages. This was done during each measurement campaign from which a mean $k_{pol,Q}$ of 1.0006 for the TM30013 and 1.0010 for the FC65G was calculated. k_{pol} listed in Table 12 is given as the ratio of the polarity correction factors at beam qualities Q and Q_0. The values for k_{pol,Q_0} were taken from the IC's calibration certificates. The standard deviation of k_{pol} of 0.08 % was estimated from the deviation of the repeated measurements performed at beam quality Q of 0.06 % and an assumed standard uncertainty of k_{pol,Q_0} of 0.05 %

Saturation effect Measurements were performed at 10 different voltages (both positive and negative) for each chamber, the inverse mean measured value $1/M$ was plotted against the inverse voltage $1/U$ as shown in Figure 31. These data sets were fitted according to Equation 45, based on which $k_{s,Q}$ was determined using Equation 46. For the TM30013 $k_{s,Q}$ is 1.0018, for the FC65G it is 1.0046. The relative standard uncertainty of both values is 0.20 %, determined based on the uncertainty of the yielded fitting parameters, also taking the standard deviation of the repeated measurements into account. k_s is then given by the ratio of $k_{s,Q}$ and $k_{s,Q_0} = 1.001$ at beam quality Q_0.

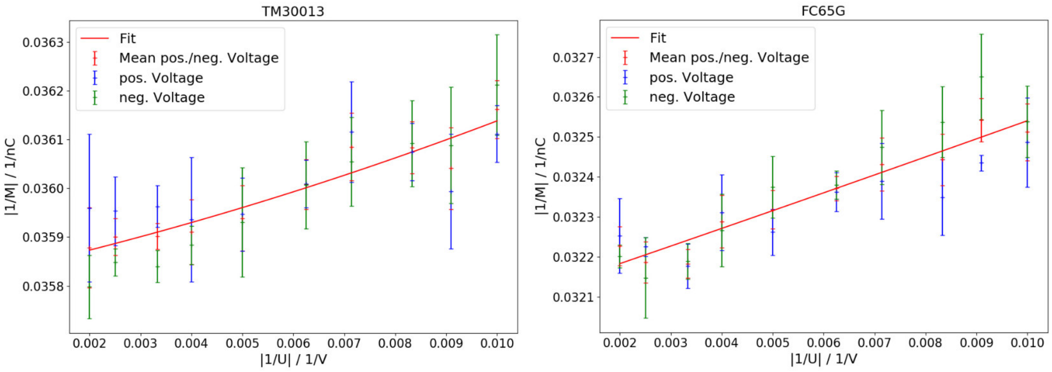

Figure 31: Plot of the inverse IC reading $1/M$ as a function of the inverse chamber voltage $1/U$, fitted with a Equation 45 to determine $k_{s,Q}$. The data was measured with the TM30013 (left) and the FC65G (right) at positive (blue) and negative voltages (green), the mean value of both voltages is shown in red. Error bars give the standard deviation of the repeated measurements. Reprinted from [3].

Volume effect Due to the flat dose of the reference ^{60}Co field, $k_{v,Q_0} = 1$ and $k_v = k_{v,Q}$. To determine $k_{v,Q}$, the dose distribution across the IC's cross section, which was taken from the field characterization measurements, was numerically integrated. Two different methods were tested for the integration: To simply sum up all measurement points which lie inside the IC's volume, and to interpolated the dose values and integrate the resulting distribution. A difference between both methods of only 0.004 % was found. The ratio of the dose value at the center of chamber's reference point and the integration result was calculated. This was done for every field characterization measurement performed before the respective measurement campaign, an individual k_v was calculated for each campaign. This was additionally done for all the other field characterization measurements; the standard deviation of all k_v values found was calculated. The standard uncertainty of k_v was determined based on this standard deviation as it addresses the influence of possible dose fluctuations, adding an additional uncertainty contribution of 0.1 %, which includes the effect of a positioning uncertainty of the IC and the assumptions that had to be made due to the lack of an IC's spatial dose response function in carbon-ion beams. The determined k_v given in the table is valid for both ICs as they have nearly the same active volume.

5.3 Determination of k_Q factors

k_Q factors for each IC were calculated according to Equation 21 based on the data and correction factors presented above. k_Q factors were calculated for each measurement campaign individually, they are shown in Figure 32.

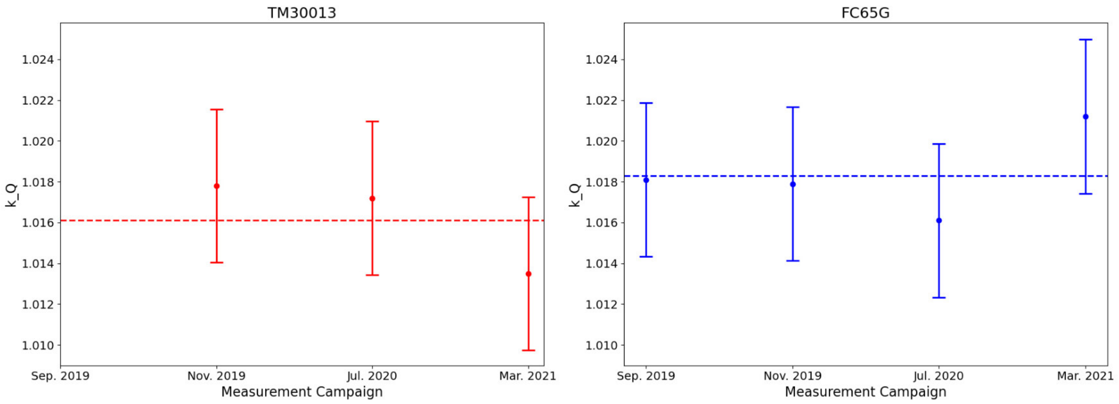

Figure 32: Resulting experimental k_Q values for each measurement campaign for the TM30013 (red) and the FC65G (blue) with their mean values indicated by the dashed lines. Error bars show the uncertainty of each k_Q value due to deviations between each experiment. Reprinted from [3].

The error bars show a relative standard uncertainty of the given k_Q values of 0.4 % for both chambers. This was calculated only including influencing quantities that depend on the given measurement situation; quantities that stay constant between the single measurements, such as N_{D,w,Q_0} or c_p, are not included. This allows a better comparison of the factors from the different measurement campaigns.
Based on the k_Q values presented, the mean was calculated for both ICs as final experimental k_Q factors. These were then compared to the values listed in TRS-398 and DIN 6801-1. An overall uncertainty budget for k_Q including all influencing quantities and valid for both chambers was established.

5.3.1 k_Q factors according to DIN / TRS

To be able to compare the experimental k_Q factors with factors given in the literature, the experimental values were expressed according to TRS-398 and DIN 6801-1 (see Chapter 2.2.4). They are given in Table 13 and shown in Figure 33 in comparison with the values stated in TRS-398 and DIN 6801-1. The given relative standard uncertainty of 0.69 % for the experimental k_Q is presented in detail in the following Chapter 5.3.2.

		TM30013 (PTW)			FC65G (IBA)	
	Calorimetry	Literature	Δ / %	Calorimetry	Literature	Δ / %
TRS	1.016 (0.69 %)	1.032 (2.8 %)	1.55	1.018 (0.69 %)	1.042 (2.8 %)	2.31
DIN	1.007 (0.69 %)	1.014 (2.2 %)	0.70	1.009 (0.69 %)	1.012 (2.2 %)	0.29

Table 13: Comparison of the determined experimental k_Q factors with values listed in TRS-398 [10] and DIN 6801-1 [13]. Experimental values are expressed according to the procedure described in TRS/DIN. Relative standard uncertainties are given in parentheses.

5.3.2 Uncertainty budget

The overall standard uncertainty for k_Q was determined within an uncertainty budget including all influencing quantities of the k_Q determination procedure. The budget was calculated according to the Guide to the Expression of Uncertainty in Measurement (GUM) [103] using the software GUM workbench [104], it is given in Table 14. As the uncertainty contribution for the two ICs were quite similar, the budget is valid for both of them.

For k_Q, the overall standard uncertainty results to 0.69 %, which is mainly defined by the uncertainty of the determined absorbed dose to water $D_{w,Q}$ and the corrected IC reading M_Q. These include the uncertainties of their influencing quantities such as the measured values and correction factors. The uncertainty of the chamber-specific calibration factor N_{D,w,Q_0} determined at the PTB primary standard, as well as the uncertainty contribution due to its time stability of 0.10 % also contribute to the overall 0.69 %. An uncertainty contribution due to temporal fluctuations in dose application was also considered, it was determined as the relative standard deviation of the repeated IC measurements in the mono-energetic beam at the isocenter (see Chapter 4.4).

From Equation 21 it can be recognized that the water calorimetry specific contributions to the overall uncertainty (marked with a *) are correlated, as N_{D,w,Q_0} and $D_{w,Q}$ are both based on water calorimetry. Taking this correlation into account, the contribution of the uncertainty of $D_{w,Q}$ to the overall standard uncertainty of k_Q is reduced to 0.53 %, for the uncertainty contribution of N_{D,w,Q_0} a value of 0.20 % has to be used.

The standard uncertainty of the absorbed dose to water $D_{w,Q}$ is determined by the thermistors' sensitivity S and the measured quantities ΔR and R, based on which the temperature rise ΔT was calculated. The contribution of 0.08 % to consider the uncertainty of the determination method for ΔR was determined as the maximum deviation from the actual ΔR when varying the time window for the linear interpolation of the signal before and after the irradiation by ±2 s. To analyse the temperature background drift, the calorimetric signal was linearly interpolated over a course of 60 s at varying positions right before the beginning of a new block of irradiations. The standard deviation of the obtained slopes' values was calculated, its influence on ΔR was considered as the uncertainty contribution of the temperature background drift. A positioning uncertainty of the calorimeter of 0.5 mm influencing the correction for the lateral displacement k_l and the measurement depth k_d was included.

For the ionometric measurements, the standard uncertainty of the corrected IC reading, resulting from the standard deviation of repeated IC measurements, as well as the uncertainties of the different correction factors contribute. The uncertainty of the measurement of temperature and air pressure was also considered, as well as a positioning uncertainty of the calorimeter itself of 0.5 mm and of the IC inside the calorimeter of an additional 0.5 mm. The uncertainty contribution of 0.03 % was determined as the maximum effect of a misalignment of 1 mm on the ionometric correction factor k_v.

Quantity	Rel. standard uncertainty / %
Calorimetric measurements	
Absorbed dose to water $D_{w,Q}$	**0.55 (0.53)**
Temperature rise ΔT	0.33
Resistance change ΔR	0.20
Thermistor's resistance R	0.02
Thermistor calibration S	0.07
Uncertainty of the determination method for ΔR	0.08
Uncertainty contribution due to a temperature background drift	0.24
Specific heat capacity of water c_p	0.03*
Correction for heat conduction effects k_c	0.40
Correction for heat defect k_h	0.14*
Correction for lateral displacement k_l	0.14
Correction for measurement depth at 4°C k_d	0.10
Correction for field perturbation by the detector k_p	0.11
Correction for thermistor's electrical power k_e	0.01
Positioning uncertainty of the calorimeter	0.06
Ionometric measurements	
Corrected IC reading M_Q	**0.32**
Air-density corrected IC reading M_{corr}	0.04
Uncertainty of the measurement of temperature and air pressure	<0.01
Correction for polarity effect k_{pol}	0.08
Air-density corrected IC reading at a negative voltage M_{neg}	0.06
Correction for polarity effect in Q_0 k_{pol,Q_0}	0.05
Correction for saturation effect $k_{s,Q}$	0.20
Correction for volume effect k_v	0.21
Uncertainty of the determination method for k_v	0.10
Positioning uncertainty of the calorimeter and the IC	0.03
Calibration factor for IC N_{D,w,Q_0}	0.25* (0.20)
Time stability of N_{D,w,Q_0}	0.10
Uncertainty contribution due to temporal fluctuations in dose application	0.21
Correction factor for beam quality k_Q	**0.69**

Table 14: Combined standard measurement uncertainty budget for the determination of k_Q. Water calorimetry specific and therefore correlated contributions are marked with a *. For $D_{w,Q}$ and N_{D,w,Q_0}, the overall standard uncertainty is given if considering all influencing quantities, as well as their contribution to the overall standard uncertainty of k_Q with considering the correlations (values in parentheses).

6 Discussion and Conclusion

For the water calorimetric determination of the absorbed dose to water, a homogeneous irradiation field of sufficient dose and size irradiated in a short time is needed. This poses a challenge when it comes to measure at a carbon-ion SOBP provided at an intensity-modulated raster scanning facility such as HIT. Nevertheless, introducing the 2DRM, a 1.5 Gy dose cube of $6 \times 6 \times 6\,\text{cm}^3$ could be irradiated within 90 s. Optimizing the 2DRM and the irradiation plan, a relative standard deviation $\leq$1.1 % of measured dose values with a maximum distance of 20 mm from the center of the distribution was achieved, proving a homogeneous dose distribution around the calorimetric measurement position. These dose values showed a mean deviation of 0.26 % for repeated measurements over a period of 10 weeks, which indicates a good time stability of the irradiation field.
EBT3 film measurements were performed to measure lateral dose distributions with a high spatial resolution. The successful application of the triple channel analysis to carbon ion-irradiated film was presented within this thesis for the first time. This correction of the resulting dose distribution significantly improved the image quality, allowing the detailed investigation of the 2DRM-induced pin pattern in the lateral dose distribution. Comparing the corrected film dose distribution with dose distributions simultaneously measured with the IC array Octavius, the sufficient Octavius' spatial resolution for the field characterization was assured.
Particle spectra were determined by means of Monte Carlo simulations for the passively modulated 2DRM SOBP and an actively scanned SOBP. The small deviations found between both irradiation modalities indicate a very similar beam quality and therefore give a good rationale to transfer the results concerning new k_Q factors also to irradiation fields created by active scanning.

Performing calorimetric and ionometric measurements, k_Q factors were determined in the SOBP of a carbon-ion beam achieving a standard uncertainty below 1 %. Hereby, the quantities mostly influencing the overall uncertainty are the correction for the heat conduction with a relative standard uncertainty of 0.4 % and the standard uncertainty of the measured temperature rise of 0.3 %.
The obtained experimental values were compared to values stated in the literature (Table 13, Figure 33), differences of up to 2.3 % were found. This might indicate that the values for the stopping power ratio $(s_{w,air})_Q$ or the mean excitation energy per ion pair $(W_{air})_Q$ in carbon-ion beams, that are applied for the theoretical calculation of k_Q (Equation 23) differ from the experimental situation.Also the assumption of a perturbation factor p_Q of unity (as stated in both TRS-398 and DIN 6801-1) might be insufficient, even though a big deviation from unity is rather unlikely due to the very short ranges of the secondary electrons of carbon ion beams. Detailed MC simulations for proton beams performed by other groups [26, 106] indicate a non-negligible, but rather small chamber specific perturbation factor below 1 %.
Using the key data for stopping power ratios and $(W_{air})_Q$ presented in the ICRU 90 report [29], a change in k_Q compared to the values stated in TRS-398 of -0.5 % can be concluded. This reduces the differences to the experimental values presented here to

1.04 % for the TM30013 and 1.80 % for the FC65G. If only the new values for $(W_{air})_Q$ are applied for the calculation of k_Q and $(s_{w,air})_Q$ is still calculated as prescribed in DIN 6801-1, a change in k_Q of $-0.1\,\%$ compared to the values stated there follows. This leads to differences to the experimental k_Q values of 0.60 % for the TM30013 and 0.18 % for the FC65G.

Within the new version of TRS-398 which which is currently in progress [49], the value from ICRU 90 for $(W_{air})_Q$ of 34.71 J/C is adapted, the value for $(s_{w,air})_Q$ is changed to 1.126. Both are still taken to be independent of the beam quality. If experimental data is available, k_Q is given as the mean between calculated and experimental value. For the TM30013 and the FC65G, the experimental values determined by Osinga *et al.* [30] are considered. This changes the k_Q value for the TM30013 to 1.037, increasing the differences to the value determined for the SOBP to 2.04 %. For the FC65G, a k_Q of 1.034 is given, which means a decreased difference of 1.53 % to the experimental SOBP value. The values stated in the new version of TRS-398 are shown as light blue dashed lines in Figure 33. However, more experimental data is needed for a reliable comparison of experiment and literature.

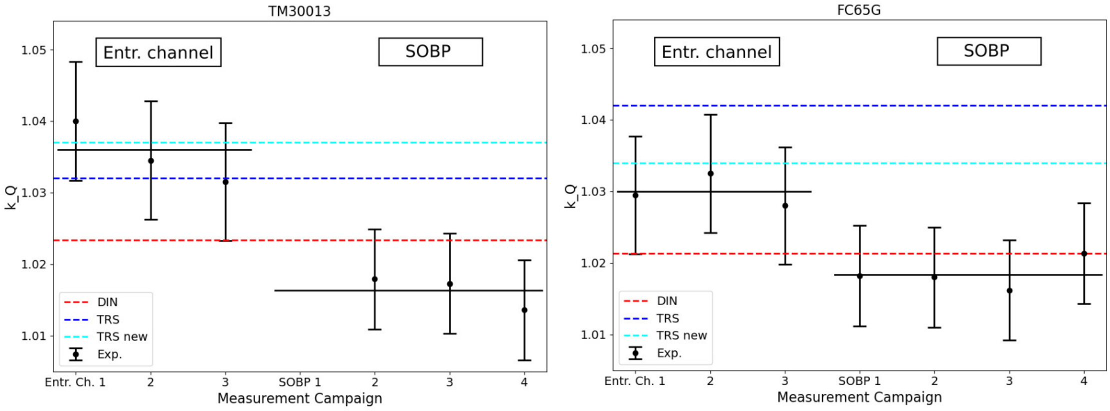

Figure 33: Experimental k_Q factors for the entrance channel [30] and the SOBP in comparison with the values stated in DIN 6801-1 [13], TRS-398 [10] and the updated TRS-398 [49] (dashed lines) for the PTW TM30013 (left) and the IBA FC65G (right). Thick lines show the mean experimental value, error bars give the corresponding combined overall standard uncertainties. The experimental values are calculated according to TRS using Equation 25, the value taken from the DIN was multiplied by a $k_r = 1.009$ for a better comparison with the TRS data.

The k_Q values determined in the SOBP were also compared to the experimental factors for the entrance channel [30] that were also determined at HIT using the PTB water calorimeter. A k_Q of $1.036 \pm 0.8\,\%$ was found for the TM30013 and $1.030 \pm 0.8\,\%$ for the FC65G (values expressed according to TRS-398), which means a difference of 1.9 % for the TM30013 and 1.1 % for the FC65G compared to the SOBP. The comparison can be seen in Figure 33. These differences might be explained by a possible LET-dependence of k_Q.

According to DIN 6801-1 [13], $(W_{air})_Q$ and p_Q remain constant when comparing the entrance channel and the SOBP, while the stopping power ratio changes as it is calculated as a function of the residual range (Equation 24). This means, the difference in k_Q between the entrance channel and the SOBP would only be determined by the difference in $(s_{w,air})_Q$ for both situations. The stopping power ratios for the entrance channel and the SOBP were calculated according to Equation 24, but using the parameter values derived by Burigo *et al.* [28], as they are based on the newer key data from ICRU 90 [29]. The comparison of the resulting stopping power values predicts a 0.3 % larger k_Q for the SOBP, whereas in this study, a up to 1.9 % decreased k_Q values was found for the SOBP. This might indicate that the assumption of constant values for $(W_{air})_Q$ and p_Q is insufficient.

If using the values for $(W_{air})_{Q_0}$, $(s_{w,air})_{Q_0} \cdot p_{Q_0}$ and $(s_{w,air})_Q$, p_Q stated in TRS-398 [10], a value of 33.96 J/C can be calculated for $(W_{air})_Q$ based on the experimental k_Q values determined within this thesis. This means a reduction of 1.6 % compared to the value of 34.5 J/C stated in TRS-398. In contrast, increased W_{air} values were obtained in different studies using monoenergetic carbon ion beams: Rossomme *et al.* [107] determined a value of 35.5 J/C for an initial beam energy of 80 MeV/u, which means an increase of about 3 % compared to the TRS value; a similar value of 35.72 J/C was found by Sakama *et al.* [108] using initial beam energies between 135 MeV/u and 430 MeV/u. Both studies were based on graphite calorimetry. Osinga *et al.* [30] calculated a value of 34.62 J/C based on the water calorimetric experiments using an IC TM30013 and an initial beam energy of 270.55 MeV/u. This comparison shows that a further investigation of the LET dependence of W_{air} is advisable.

An additional experiment was carried out within this thesis performing water calorimetric and ionometric measurements in the entrance channel of the monoenergetic irradiation field (i.e. using the same irradiation plan as described in Chapter 3.1.4 but without 2DRM in the beam path). Hereby, a measurement depth of 5 cm inside the water calorimeter was choosen as it was also done by Osinga *et al.* [30]. This gives the advantage of an identical initial beam energy and scanning scheme compared to the experiments in the SOBP, leading to similar correction factors. Comparing the results with the ones from the SOBP measurements, a similar trend can be seen as in the comparison with the values found by Osinga *et al.*: The k_Q factors determined for the entrance channel are between 0.6 % and 2.6 % higher than the factors found for the SOBP. Though, this experiment has to be repeated for a reliable comparison.

A comparison of the water calorimetric experiment presented here with graphite calorimetry would be favorable as this offers the opportunity of an independent verification of the results obtained. Compared to water calorimetry, graphite calorimetry offers the advantage of better heat conduction which makes the system's thermal behaviour easier to model for a known specific heat capacity of graphite [109]. On the other hand, an absorbed dose to graphite is measured which has to be converted into absorbed dose to water adding an additional uncertainty of the dose conversion procedure. However, the resulting overall standard uncertainties of graphite and water calorimetric experiments are comparable [109].

With the work presented in this thesis, k_Q values are now available for the SOBP for the first time. Their small standard uncertainty of 0.69 % offers the possibility of a substantial reduction of the uncertainty in dosimetry for carbon-ion beams. Nevertheless, an enlargement of the data base is still desirable. Also a further investigation of a possible LET-dependence of k_Q is needed.

7 Appendix

References

[1] K.M. Holm, U. Weber, Y. Simeonov, A. Krauss, O. Jäkel, and S. Greilich. 2D range modulator for high-precision water calorimetry in scanned carbon-ion beams. *Physics in Medicine and Biology*, 65:215003, 2020.

[2] K.M. Holm, E. Yukihara, M.F. Ahmed, S. Greilich, and O. Jakel. Triple channel analysis of Gafchromic™ EBT3 irradiated with clinical carbon-ion beams. *submitted to Physica Medica*, 2020.

[3] K.M. Holm, O. Jakel, and A. Krauss. Water calorimetry-based kQ-factors for Farmer-type ionization chambers in the SOBP of a carbon-ion beam. *submitted to Physics in Medicine and Biology*, 2021.

[4] U. Amaldi and G. Kraftr. Radiotherapy with beams of carbon ions. *Reports on Progress in Physics*, 68:1861, 2005.

[5] M. Lodge, M. Pijls-Johannesma, L. Stirk, A. Munro, D. De Ruysscher, and T. Jefferson. A systematic literature review of the clinical and cost-effectiveness of hadron therapy in cancer. *Radiotherapy and Oncology*, 83:110, 2007.

[6] C. Karger, O. Jakel, H. Palmans, and T. Kanai. Dosimetry for ion beam radiotherapy. *Physics in Medicine and Biology*, 55:R193, 2010.

[7] T. Kamada, H. Tsujii, E. Blakley, J. Debus, W. De Neve, M. Durante, o. Jäkel, R. Mayer, R. Orecchia, R. Pötter, S. Vatnitsky, and W. Chu. Carbon ion radiotherapy in Japan: an assessment of 20 years of clinical experience. *Lancet Oncology*, 16:e93, 2015.

[8] D. Schulz-Ertner, Anna Nikoghosyan, C. Thilmann, T. Haberer, O. Jäkel, C. Karger, G. Kraft, M. Wannenmacher, and J. Debus. Results of carbon ion radiotherapy in 152 patients. *International Journal of Radiation Oncology Biology Physics*, 58(2):631, 2004.

[9] M. Durante and J. Loeffler. Charged particles in radiation oncology. *Nature Reviews Clinical Oncology*, 7:37, 2009.

[10] P. Andreo, D. Burns, K. Hohlfeld, M. Saiful Huq, T. Kanai, F. Laitano, V. Smyth, and S. Vynckier. Absorbed Dose Determination in External Beam Radiotherapy: an International Code of Practice for Dosimetry Based on Standards of Absorbed Dose to Water (IAEA TRS-398, V.12). *International Atomic Energy Agency, Vienna*, 2006.

[11] M. Mitch, L. DeWerd, R. Minniti, and J. Williamson. Treatment of Uncertainties in Radiation Dosimetry. *Clinical Dosimetry Measurements in Radiotherapy (AAPM), Chapter 22*, page 737, 2009.

[12] J. Van Dyk, J Battista, and G. Baumann. Accuracy and Uncertainty Considerations in Modern Radiation Oncology. *The Modern Technology of Radiation Oncology, Chapter 11*, 3:378, 2013.

[13] DIN-Normenausschuss Radiologie (NAR). DIN 6801-1: Dosismessverfahren nach der Sondenmethode für Protonen- und Ionenstrahlung - Teil 1: Ionisationskammern. *DIN Deutsches Institut für Normung e. V.*, 2016.

[14] P. Andreo, D.T. Burns, R.P. Kapsch, M. McEwen, S. Vatnitsky, C.E. Andersen, F. Ballester, J. Borbinha, F. Delaunay, P. Francescon, M.D. Hanlon, L. Mirzakhanian, B. Muir, J. Ojala, C.P. Oliver, M. Pimpinella, M. Pinto, L.A. de Prez, J. Seuntjens, L. Sommier, P. Teles, J. Tikkanen, J. Vijande, and K. Zink. Determination of consensus kQ values for megavoltage photon beams for the update of IAEA TRS-398. *Physics in Medicine and Biology*, 65(9):095011, 2020.

[15] A. Krauss, L. Buermann, H.-M. Kramer, and H.-J. Selbach. Calorimetric determination of the absorbed dose to water for medium-energy x-rays with generating voltages from 70 to 280 kV. *Physics in Medicine and Biology*, 57:2523, 2012.

[16] A. Krauss and R. Kapsch. Calorimetric determination of kQ factors for NE 2561 and NE 2571 ionization chambers in 5 cm × 5 cm and 10 cm × 10 cm radiotherapy beams of 8 MV and 16 MV photons. *Physics in Medicine and Biology*, 52:2523, 2007.

[17] M.R. McEwen. Measurement of ionization chamber absorbed dose factors in megavoltage photon beams. *Medical Physics*, 37(5):2179–2193, 2010.

[18] A. Krauss and R. Kapsch. Experimental determination of kQ factors for cylindrical ionization chambers in 10 cm × 10 cm and 3 cm × 3 cm photon beams from 4 MV to 25 MV. *Physics in Medicine and Biology*, 59:035041, 2014.

[19] A. Krauss and R. Kapsch. Direct determination of kQ factors for cylindrical and plane-parallel ionization chambers in high-energy electron beams from 6 MeV to 20 MeV. *Physics in Medicine and Biology*, 63:2523, 2018.

[20] J. Medin, C.K. Ross, N.V. Klassen, H. Palmans, E. Grusell, and J.-E. Grindborg. Experimental determination of beam quality factors, kQ, for two types of Farmer chamber in a 10 MV photon and a 175 MeV proton beam. *Physics in Medicine and Biology*, 51:1503, 2006.

[21] J. Medin. Implementation of water calorimetry in a 180 MeV scanned pulsed proton beam including an experimental determination of kQ for a Farmer chamber. *Physics in Medicine and Biology*, 55:3287, 2010.

[22] J. Wulff, J.T. Heverhagen, and K. Zink. Monte-Carlo-based perturbation and beam quality correction factors for thimble ionization chambers in high-energy photon beams. *Physics in Medicine and Biology*, 53(11):2823–2836, 2008.

[23] B.R. Muir and D.W.O. Rogers. Monte Carlo calculations of kQ, the beam quality conversion factor. *Medical Physics*, 37(11):5939–5950, 2010.

[24] K Zink and J Wulff. Beam quality corrections for parallel-plate ion chambers in electron reference dosimetry. *Physics in Medicine and Biology*, 57(7):1831–1854, 2012.

[25] B.R. Muir and D.W.O. Rogers. Monte Carlo calculations of electron beam quality conversion factors for several ion chamber types. *Medical Physics*, 41(11):111701, 2014.

[26] C. Goma, P. Andreo, and J. Sempau. Monte Carlo calculation of beam quality correction factors in proton beams using detailed simulation of ionization chambers. *Physics in Medicine and Biology*, 61:2389, 2016.

[27] H.J. Brede, K.-D. Greif, O. Hecker, P. Heeg, D.T.L. Jones, H. Kluge, and D. Schardt. Absorbed dose to water determination with ionization chamber dosimetry and calorimetry in restricted neutron, photon, proton and heavy-ion radiation fields. *Physics in Medicine and Biology*, 51:3663, 2006.

[28] L.N. Burigo and S. Greilich. Impact of new ICRU 90 key data on stopping-power ratios and beam quality correction factors for carbon ion beams. *Physics in Medicine and Biology*, 64:195005, 2019.

[29] S.M. Seltzer, J.M. Fernández-Varea, P. Andreo, P.M. Bergstrom Jr., D.T. Burns, I. Krajcar, C.K. Ross, and F. Salvat. ICRU Report No. 90: Key data for ionizing-radiation dosimetry: Measurement standards and applicсations. *Journal of the ICRU*, 14(1), 2016.

[30] J.-M. Osinga-Blättermann, S. Brons, S. Greilich, O. Jäkel, and A. Krauss. Direct determination of kQ for Farmer-type ionization chambers in a clinical scanned carbon ion beam using water calorimetry. *Physics in Medicine and Biology*, 62:2033, 2017.

[31] A. Krauss. The PTB water calorimeter for the absolute determination of absorbed dose to water in 60Co radiation. *Metrologia*, 43:259, 2006.

[32] J.-M. Osinga-Blättermann and A. Krauss. Determination of kQ factors for cylindrical and plane-parallel ionization chambers in a scanned carbon ion beam by means of cross calibration. *Physics in Medicine and Biology 107683.R1*, 2018.

[33] O. Jäkel, G. H. Hartmann, C. P. Karger, P. Heeg, and S. Vatnitsky. A calibration procedure for beam monitors in a scanned beam of heavy charged particles. *Medical Physics*, 31(5):1009–1013, 2004.

[34] O.Jäkel W. Schlegel, C. Karger. *Medizinische Physik*. Springer Spektrum, Berlin, 1 edition, 2018.

[35] Hanno Krieger. *Grundlagen der Strahlungsphysik und des Strahlenschutzes.* Springer Spektrum, Wiesbaden, 4 edition, 2012.

[36] H. Bethe. Zur Theorie des Durchgangs schneller Korpuskularstrahlen durch Materie. *Annalen der Physik*, 397(3):325–400, 1930.

[37] Gert Molière. Theorie der Streuung schneller geladener Teilchen I: Einzelstreuung am abgeschirmten Coulomb-Feld. *Zeitschrift für Naturforschung*, 2a:133, 1947.

[38] Gert Molière. Theorie der Streuung schneller geladener Teilchen II: Mehrfach- und Vielfachstreuung. *Zeitschrift für Naturforschung*, 3a:78, 1948.

[39] M. Krämer, O. Jäkel, T. Haberer, G. Kraft, D. Schardt, and U. Weber. Treatment planning for heavy-ion radiotherapy: physical beam model and dose optimization. *Physics in Medicine and Biology*, 45(11):3299–3317, 2000.

[40] O. Jäkel, C. Jacob, D. Schardt, C.P. Karger, and G.H. Hartmann. Relation between carbon ion ranges and x-ray CT numbers. *Medical Physics*, 28(4):701–703, 2001.

[41] Hanno Krieger. *Strahlungsmessung und Dosimetrie.* Springer Spektrum, Wiesbaden, 2 edition, 2013.

[42] DIN-Normenausschuss Radiologie (NAR). DIN 6800-1: Dosismessverfahren nach der Sondenmethode für Photonen- und Elektronenstrahlung - Teil 1: Allgemeines. *DIN Deutsches Institut für Normung e. V.*, 2016.

[43] L.V. Spencer and F.H. Attix. A Theory of Cavity Ionization. *Radiation Research*, 3(3):239–254, 1955.

[44] L.V. Spencer and F.H. Attix. A Cavity Ionization Theory Including the Effects of Energetic Secondary Electrons. *Radiology*, 64(1):113–113, 1955.

[45] E.W. Lemmon, M.O. McLinden, and D.G. Friend. *Thermophysical Properties of Fluid Systems.* NIST Chemistry WebBook, NIST Standard Reference Database Number 69, 2021.

[46] M. Sassowsky and E. Pedroni. On the feasibility of water calorimetry with scanned proton radiation. *Physics in Medicine and Biology*, 50:5381, 2005.

[47] A. Krauss. Heat conduction effects during the calorimetric determination of absorbed dose to water in radiotherapy beams. *Thermochimica Acta*, 445:126, 2006.

[48] H. Palmans, L. Nafaa, J. De Jans, S. Gillis, M.-T. Hoornaert, C. Martens, M. Piessens, H. Thierens, A. Van der Plaetsen, and S. Vynckier. Absorbed dose to water based dosimetry versus air kerma based dosimetry for high-energy photon beams: an experimental study. *Physics in Medicine and Biology*, 47:421, 2002.

[49] O. Jäkel. Personal communication 01/21.

[50] Stabsstelle für Presse-und Öffentlichkeitsarbeit des Universitätsklinikums Heidelberg und der Medizinischen Fakultät der Universität Heidelberg. Das Heidelberger Ionenstrahl-Therapiezentrum (Informationsbroschüre). *https://www.klinikum.uni-heidelberg.de/*, accessed 11/01/21.

[51] T. Haberer, J. Debus, H. Eickoff, O. Jäkel, D. Schulz-Ertner, and U. Weber. The Heidelberg ion therapy center. *Radiotherapy and Oncology*, 73(2):S186, 2004.

[52] T. Haberer, W. Becher, D. Schardt, and G. Kraft. Magnetic scanning system for heavy ion therapy. *Nuclear Instruments and Methods in Physics Research Section A*, 330:296, 1993.

[53] Uli Weber and Gerhard Kraft. Design and construction of a ripple filter for a smoothed depth dose distribution in conformal particle therapy. *Physics in Medicine and Biology*, 44(11):2765–2775, 1999.

[54] Y. Simeonov, U. Weber, P. Penchev, T. Ringbæk, C. Schuy, S. Brons, R. Engenhart-Cabillic, J. Bliedtner, and K. Zink. 3D range-modulator for scanned particle therapy: development, Monte Carlo simulations and experimental evaluation. *Physics in Medicine and Biology*, 62:7075, 2017.

[55] V. Kostjuchenko, D. Nichiporov, and V. Luckjashin. A compact ridge filter for spread out Bragg peak production in pulsed proton clinical beams. *Medical Physics*, 28(7):1427, 2001.

[56] F. Tommasino, M. Rovituso, E. Bortoli, C. La Tessa, G. Petringa, S. Lorentini, E. Verroi, Y. Simeonov, U. Weber, P. Cirrone, M. Schwarz, M. Durante, and E. Scifoni. A new facility for proton radiobiology at the Trento proton therapy centre: Design and implementation. *Physica Medica*, 58:99, 2019.

[57] O. Jakel, G.H. Hartmann, C.P. Karger, P. Heeg, and J. Rassow. Quality assurance for a treatment planning system in scanned ion beam therapy. *Medical Physics*, 27(7):1588, 2000.

[58] M.J. Butson, P.K.N. Yu, T. Cheung, and P. Metcalf. Radiochromic film for medical radiation dosimetry. *Materials Science and Engineering*, 41:61, 2003.

[59] Gafchromic. Gafchromic™ EBT3 Dosimetry Film Specifications. *http://www.gafchromic.com/*, accessed 03/29/19.

[60] M.A. Stevens, J.R. Turner, R.P. Hugtenburg, , and P.H. Butler. High-resolution dosimetry using radiochromic film and a document scanner. *Physics in Medicine and Biology*, 41:2357, 1996.

[61] C. Goma, P. Andreo, and J. Sempau. Spencer–Attix water/medium stopping-powerratios for the dosimetry of proton pencil beams. *Physics in Medicine and Biology*, 58:2509, 2013.

[62] L. J. van Battum, D. Hoffmans, H. Piersma, and S. Heukelom. Accurate dosimetry with Gafchromic™ EBT film of a photon beam in water: What level is achievable? *Medical Physics*, 35(2):704–716, 2008.

[63] B. Hartmann, M. Martišíková, and O. Jäkel. Technical Note: Homogeneity of Gafchromic® EBT2 film. *Medical Physics*, 37(4):1753–1756, 2010.

[64] A. Micke, D. Lewis, and X. Yu. Multichannel film dosimetry with nonuniformity correction. *Medical Physics*, 38(5):2523, 2011.

[65] R. Mayer, F. Ma, R. Miller, A. Belard, J. McDonough, and J. O'Connell. Enhanced dosimetry procedures and assessment for EBT2 radiochromic film. *Medical Physics*, 39(4):2147, 2012.

[66] I. Mendez, P. Peterlin, R. Hudej, A. Strojnik, and B. Casar. On multichannel film dosimetry with channel-independent perturbations. *Medical Physics*, 41:011705, 2014.

[67] I. Mendez. Model selection for radiochromic film dosimetry. *Physics in Medicine and Biology*, 60:4089, 2015.

[68] N. Hayashi, Y. Watanabe, R. Malmin, and H. Kato. Evaluation of triple channel correction acquisition method for radiochromic film dosimetry. *Journal of Radiation Research*, 53(6):930, 2012.

[69] S.J. van Hoof, P.V. Granton, G. Landry, M. Podesta1and, and F. Verhaegen. Evaluation of a novel triple-channel radiochromic film analysis procedure using EBT2. *Physics in Medicine and Biology*, 57:4353, 2012.

[70] Y. Li, L. Chen, J. Zhu, and X. Liu. The combination of the error correction methods of Gafchromic EBT3 film. *Plos One*, 12(7), 2017.

[71] A. Palmer, D. Bradley, and A. Nisbet. Evaluation and implementation of triple-channel radiochromic film dosimetry in brachytherapy. *Journal of Applied Clinical Medical Physics*, 15(4):280, 2014.

[72] R. Castriconi, M. Ciocca, A. Mirandola, C. Sini, S. Broggi, M. Schwarz, F. Fracchiolla, M. Martišíková, G. Aricò, G. Mettivier1, and P. Russo. Dose–response of EBT3 radiochromic films to proton and carbon ion clinical beams. *Physics in Medicine and Biology*, 62:377, 2017.

[73] M. Martišíková and O. Jäkel. Dosimetric properties of Gafchromic® EBT films in monoenergetic medical ion beams. *Physics in Medicine and Biology*, 55:3741, 2010.

[74] M. Martišíková and O. Jäkel. Dosimetric properties of Gafchromic® EBT films in medical carbon ion beams. *Physics in Medicine and Biology*, 55:5557, 2010.

[75] A. Niroomand-Rad, C.R. Blackwell, B.M. Coursey, K.P. Gall, W.L. McLaughlin J.M. Galvin, A.S. Meigooni, R. Nath, J.E. Rodgers, and C.G. Soares. Radiochromic film dosimetry: Recommendations of AAPM Radiation Therapy Committee Task Group 55. *Medical Physics*, 25(11):2093, 1998.

[76] M. Fuss, E. Sturtewagen, C. De Wagter, and D. Georg. Dosimetric characterization of Gafchromic EBT film and its implication on film dosimetry quality assurance. *Physics in Medicine and Biology*, 52:4211, 2007.

[77] S Devic, J. Seuntjens, E. Sham, E.B. Podgorsak, C.R. Schmidtlein, A.S. Kirov, and G.C. Soares. Precise radiochromic film dosimetry using a flat-bed document scanner. *Medical Physics*, 32(7):2245, 2005.

[78] D. Lewis, A. Micke, and X. Yu. An efficient protocol for radiochromic film dosimetry combining calibration and measurement in a single scan. *Medical Physics*, 39(10):377, 2012.

[79] A. Palmer, D. Bradley, and A. Nisbet. Evaluation and mitigation of potential errors in radiochromic film dosimetry due to film curvature at scanning. *Journal of Applied Clinical Medical Physics*, 16(2):425, 2015.

[80] The ImageMagick Development Team. Imagemagick (vers. 7.0.10). *https://imagemagick.org*, accessed 12/01/20.

[81] K. Alexander. Development of a Novel Readout System for Radiochromic Film Dosimetry. Master's thesis, Department of Physics, Engineering Physics and Astronomy, Queen's University Kingston, Canada, 2014.

[82] S. Devic, S. Aldelaijan, H. Mohammed, N. Tomic, L.-H. Liang, F. DeBlois, and J. Seuntjens. Absorption spectra time evolution of EBT-2 model Gafchromic™ film. *Medical Physics*, 37(5):2207, 2010.

[83] NumPy community. NumPy Reference, Release 1.16.1. *http://docs.scipy.org/doc/numpy-1.16.1/numpy-ref-1.16.1.pdf*, accessed 03/29/19.

[84] A. Clark and Contributors. Pillow (PIL fork) Documentation, Release 5.4.1. *http://media.readthedocs.org/pdf/pillow/stable/pillow.pdf*, accessed 03/29/19.

[85] E. Jones, T. Oliphant, P. Peterson, et al. SciPy: Open source scientific tools for Python. *http://www.scipy.org/*, accessed 03/29/19.

[86] D.A. Low, W.B. Harms, S. Mutic, and J.A. Purdy. A technique for the quantitative evaluation of dose distributions. *Medical Physics*, 25(5):656–661, 1998.

[87] D. Bauer. Study of the Octavius ionization chamber array as a film replacement for clinical ion beam quality assurance. Master's thesis, Department of Physics, University of Heidelberg, Germany, 2018.

[88] PTW Freiburg. Octavius 1000 SRS. *http://www.ptw.de/2287.html*, accessed 04/04/19.

[89] C. Schuy, Y. Simeonov, M. Durante, K. Zink, and U. Weber. Technical journal: Vendor-agnostic water phantom for 3D dosimetry of complex fields in particle therapy. *Journal of Applied Clinical Medical Physics*, 21(10):227–232, 2020.

[90] R.J. Maarks. *Introduction to Shannon Sampling and Interpolation Theory.* Springer, New York, 1991.

[91] Alexander D. Poularikas. *Handbook of Formulas and Tables for Signal Processing.* Springer-Verlag, Berlin, 1 edition, 1999.

[92] PTW Freiburg. Particle Therapy QA Tools. *https://www.ptwdosimetry.com/en/products/peakfinder/*, accessed 08/08/19.

[93] A. Ferrari, P.R. Sala, A. Fasso, and J. Ranft. Fluka: a multi-particle transport code (Program version 2014).

[94] A. Westerdiep. Online Voxelizer. *http://drububu.com/miscellaneous/voxelizer/*, accessed 07/08/19.

[95] S.R. Domen. A sealed water calorimeter for measuring absorbed dose. *Journal of Research of the National Institute of Standards and Technology*, 99:121, 1994.

[96] N.V. Klassen and C.K. Ross. Water calorimetry: The heat defect. *Journal of Research of the National Institute of Standards and Technology*, 102:63, 1997.

[97] H. Palmans, J. Seuntjens, F. Verhaegen, J.M. Denis, S. Vynckier, and H. Thierens. Water calorimetry and ionization chamber dosimetry in an 85 MeV clinical proton beam. *Medical Physics*, 23(5):643, 1996.

[98] PTW Freiburg. Semiflex Ionization Chamber 30013. *https://www.ptwdosimetry.com/en/products/semiflex-ionization-chamber-31013/*, accessed 09/01/20.

[99] IBA Dosimetry. Detectors for Relative and Absolute Dosimetry - Ionization Chambers and Diode Detectors. *https://www.iba-dosimetry.com/product/fc65-g-fc65-p-ionization-chambers/*, accessed 09/01/20.

[100] K. Derikum. Correcting for ion recombination effects in ionization chambers consistently in continuous and pulsed radiation. *International Atomic Energy Agency (IAEA): Standards and Codes of Practice in Medical Radiation Dosimetry*, 1:353, 2003.

[101] Hui Khee Looe, Tenzin Sonam Stelljes, Simon Foschepoth, Dietrich Harder, Kay Willborn, and Björn Poppe. The dose response functions of ionization chambers in photon dosimetry - Gaussian or non-Gaussian? *Zeitschrift für Medizinische Physik*, 23(2):129, 2013.

[102] S. Ketelhut and R.-P. Kapsch. Measurements of spatial response functions of dosimetric detectors. *Physics in Medicine and Biology*, 60:6177, 2015.

[103] Joint Committee for Guides in Metrology. Evaluation of measurement data - Guide to the expression of uncertainty in measurement. *JCGM 100:2008*, 2008.

[104] Metrodata GmbH. GUM Workbench. 2017.

[105] Y. Simeonov. Personal communication 06/19.

[106] A. Lourenço, H. Bouchard, S. Galer, G. Royle, and H. Palmans. The influence of nuclear interactions on ionization chamber perturbation factors in proton beams: Fluka simulations supported by a fano test. *Medical Physics*, 46(2):885–891, 2019.

[107] S. Rossomme, H. Palmans, R. Thomas, N. Lee, S. Duane, M. Bailey, D. Shipley, D. Bertrand, F. Romano, P. Cirrone, G. Cuttone, and S. Vynckier. Reference dosimetry for light-ion beams based on graphite calorimetry. *Radiation Protection Dosimetry*, 161(1-4):92–95, 2013.

[108] M. Sakama, T. Kanai, A. Fukumura, and K. Abe. Evaluation of w values for carbon beams in air, using a graphite calorimeter. *Physics in Medicine and Biology*, 54:1111, 2009.

[109] J.P. Seuntjens and A.R. Dusautoy. Review of calorimeter-based absorbed dose to water standards. *International Atomic Energy Agency (IAEA)*, CN(96):11–12, 2002.

List of Figures

List of Tables

8 Danksagung

Als erstes möchte ich mich bei Prof. Dr. Oliver Jäkel für die Möglichkeit bedanken in seiner Abteilung *Medizinische Physik in der Strahlentherapie* am DKFZ zu promovieren. Diese Arbeit war eine Forschungskooperation zwischen dem DKFZ und der PTB Braunschweig, die ohne Dr. Ulrike Ankerhold, Leiterin des Fachbereichs *Dosimetrie für Strahlentherapie und Röntgendiagnostik* an der PTB, nicht zustande gekommen wäre. Dafür und für ihre Unterstützung möchte ich mich auch bei ihr bedanken.
Ich bedanke mich auch bei Prof. Dr. Joao Seco, der sich als Erstgutachter für diese Arbeit zur Verfügung gestellt hat, sowie bei Prof. Dr. Christian Karger, der als Mitglied meines Thesis Advisory Committees viele gute Anregungen für die Arbeit geliefert hat.

Dann geht ein großer Dank an Dr. Achim Krauss, der diese Arbeit von Seiten der PTB betreut hat. Vielen Dank für die immer verlässliche Unterstützung, die vielen sehr hilfreichen Diskussionen und das Lesen dieser Arbeit und auch der anderen Veröffentlichungen. Ich danke auch Dr. Steffen Greilich für die Betreuung von Seiten des DKFZ und Prof. Dr. Oliver Jäkel, der diese später übernommen hat.
Innerhalb dieser Arbeit wurde das Kalorimetrie-Projekt am HIT weitergeführt, dass vor mir Dr. Julia-Maria Osinga-Blättermann begonnen hatte. Ihre sehr detaillierten und strukturierten Aufzeichnungen, die sie mir hinterlassen hat, haben mir den Einstieg in das Projekt immens erleichtert, dafür auch ein großes Dankeschön.

Ein Kernelement dieser Arbeit war der Reichweitenmodulator, der von Dr. Ulrich Weber von der GSI und Dr. Yuri Simeonov von der Technischen Hochschule Mittelhessen entwickelt wurde. Ich möchte mich bei ihnen für die Zusammenarbeit bedanken, dafür, dass sie alle meine Wünsche bezüglich des Modulators umgesetzt und dadurch erst die Kalorimetermessungen im SOBP ermöglicht haben.
Ich möchte mich auch bei Dr. Eduardo Yukihara vom PSI bedanken für seine große Hilfe bei den EBT3-Messungen.

Bei den Kalorimetermessungen wurde ich tatkräftig von meiner Arbeitsgruppe an der PTB unterstützt. Dafür möchte ich mich bei Andreas Schlesner, Karl-Heinz Misselhorn und Thomas Hackel bedanken, dafür dass sie extra für meine Messungen nach Heidelberg gekommen sind und sich mit mir diverse Nachtschichten um die Ohren geschlagen haben. Natürlich wäre das Ganze ohne Strahl nicht möglich gewesen! Daher ein großes Dankeschön an das Team von HIT und insbesondere an Dr. Stephan Brons für seine große Unterstützung und Hilfe, wann immer es Probleme bei den Bestrahlungen gab, und an das Beschleuniger-Team, die meine nächtlichen Messungen mehrfach gerettet haben, wenn es Probleme mit dem Beschleuniger gab.

Ich möchte mich auch bei der Arbeitsgruppe um Tim, Renato und Laura für die gemeinsamen Mittagessen und netten Kaffeerunden bedanken, die in dieser Hinsicht quasi eine Ersatz-Arbeitsgruppe für mich waren, als sich meine leider nach und nach aufgelöst hat.

Und der größte Dank geht natürlich an meine Familie, die mich immer unterstützt hat, besonders an meinen Papa für meinen persönlichen, immer verlässlichen IT-Support. Und an Niclas, der immer für mich da ist.

Erklärung

Ich erkläre hiermit, dass ich die vorgelegte Dissertation selbst verfasst und mich dabei keiner anderen als der von mir ausdrücklich bezeichneten Quellen und Hilfen bedient habe.

Heidelberg, den 31.03.2021

Kim Marina Holm